



저작자표시-비영리-변경금지 2.0 대한민국

이용자는 아래의 조건을 따르는 경우에 한하여 자유롭게

- 이 저작물을 복제, 배포, 전송, 전시, 공연 및 방송할 수 있습니다.

다음과 같은 조건을 따라야 합니다:



저작자표시. 귀하는 원저작자를 표시하여야 합니다.



비영리. 귀하는 이 저작물을 영리 목적으로 이용할 수 없습니다.



변경금지. 귀하는 이 저작물을 개작, 변형 또는 가공할 수 없습니다.

- 귀하는, 이 저작물의 재이용이나 배포의 경우, 이 저작물에 적용된 이용허락조건을 명확하게 나타내어야 합니다.
- 저작권자로부터 별도의 허가를 받으면 이러한 조건들은 적용되지 않습니다.

저작권법에 따른 이용자의 권리는 위의 내용에 의하여 영향을 받지 않습니다.

이것은 [이용허락규약\(Legal Code\)](#)을 이해하기 쉽게 요약한 것입니다.

[Disclaimer](#)

**Implantable and minimally-invasive drug delivery
system using soft bioelectronics for diagnosis and
treatment**

지도교수 김 대 형

이 논문을 공학박사 학위논문으로 제출함
2020년 7월

서울대학교 대학원
화학생물공학부 에너지환경화학융합기술전공
이 영 식

이영식의 공학박사 학위논문을 인준함
2020년 7월

위 원 장	성영은	(인)
부 위 원 장	김 대 형	(인)
위 원	권 태한	(인)
위 원	소 동리	(인)
위 원	최 문기	(인)

공학박사학위논문

**Implantable and minimally-invasive
drug delivery system using soft
bioelectronics for diagnosis and
treatment**

질병 진단 및 치료를 위한 부드러운
바이오소자를 기반으로 한 생체삽입
가능하며 최소침습적인 약물전달
시스템

2020년 8월

서울대학교 대학원

화학생물공학부 에너지환경화학융합전공

이 영 식

Abstract

Implantable and minimally-invasive drug delivery system using soft bioelectronics for diagnosis and treatment

Youngsik Lee

School of Chemical and Bioengineering

Chemical Convergence for Energy and Environment

The Graduate School

Seoul National University

Biomedical electronic devices, especially for drug delivery system applied for specific human body parts have attracted considerable attention among scientists and clinicians because they present significant breakthroughs to solve various clinical issues. Because, conventional materials and devices are rigid and bulky feature, mechanical mismatch between devices and human body causes significant damages on tissues. In this regard, recent innovations in soft functional materials, novel device design strategies, and clinically relevant system-level applications have accelerated the rapid growth in this

research field. Here, we describe three types of implantable and minimally-invasive drug delivery system using soft bioelectronics for disease diagnosis and treatment.

First, a soft miniaturized drug delivery implant (SMDDI) wirelessly interconnected with wearables is fabricated. The SMDDI is wirelessly powered and controlled by wearables that continuously monitor electrophysiological signals and trigger the drug-release on-demand through the wireless power transmission. Subcutaneous release of pharmaceuticals from SMDDI based on epidermal electrophysiology monitoring could treat urgent medical situations such as status epilepticus.

Second, a multifunctional endoscope-based surgical system integrating transparent graphene bio-electronics with theranostic NPs is developed. These advanced electronics and nanoparticles enable optical fluorescence-based imaging, electrical impedance and pH detecting, contact/temperature monitoring, radio frequency ablation, and localized photo/chemotherapy for a closed-loop system on colon cancer treatment.

Third, a localized delivery system of theranostic nanoparticles (NPs) and high-energy photons to target tumors by using microneedle-integrated bioelectronics for minimally-invasive cancer treatment is developed. Theranostic NPs are locally delivered to target tumor by bioresorbable microneedles. Then, light-guiding/-spreading microneedles deliver high-energy photons generated by the bioelectronics. The high-energy photons

locally activate the NPs to induce the photodynamic-/chemo-therapy in the target tumor.

Keywords: bioelectronics, implantable, minimally-invasive, wearable. drug delivery, diagnosis, treatment

Student ID: 2013-22532

Contents

Abstract	i
Contents	iv
List of Figures	vi
List of Tables	ix
Chapter 1. Recent advances in wearable, implantable, and minimally-invasive bioelectronics using functional nanomaterials	1
1.1 Introduction.....	1
1.2 Nanomaterials as a functional basis of soft electronic devices.....	3
1.3 Soft bio-integrated electronics based on functional nanomaterials.....	7
1.4 Wearable systems using soft bioelectronics.....	9
1.5 Implantable devices based on soft bioelectronics.....	13
1.6 Minimally-invasive surgical tools based on soft bioelectronics.....	16
1.7 Conclusion.....	20
References.....	21
Chapter 2. Soft miniaturized drug delivery implant wirelessly powered and controlled by wearables	32
2.1 Introduction.....	32
2.2 Experimental section.....	36

2.3 Results and discussion	39
2.4 Conclusion	55
References	56
Chapter 3. Localized delivery of theranostic nanoparticles and high-energy photons using microneedle-integrated bioelectronics for minimally-invasive cancer treatment	59
3.1 Introduction	59
3.2 Experimental section	63
3.3 Results and discussion	67
3.4 Conclusion	76
References	77
Chapter 4. Smart endoscope system integrated with transparent bioelectronics and theranostic nanoparticles for colon cancer treatment	81
4.1 Introduction	81
4.2 Experimental section	83
4.3 Results and discussion	86
4.4 Conclusion	104
References	105
국문 초록 (Abstract in Korean)	109

List of Figures

Chapter 1

Figure 1.1. Soft nanomaterials and functional applications for bioelectronics	5
Figure 1.2. Schematic illustration of wearable, implantable, and minimally invasive devices incorporating functional nanomaterials	8
Figure 1.3. Wearable bioelectronics	12
Figure 1.4. Implantable devices	15
Figure 1.5. Minimally-invasive devices	19

Chapter 2

Figure 2.1. Monitoring and treatment scenario of the epileptic medical emergency by using SMDDI	35
Figure 2.2. Wireless integration of SMDDI and wearable	42
Figure 2.3. Various types of wearable power transmitters depending on the location of SMDDI	43
Figure 2.4. Circuit design and information of microchips for the wearable sensor	44
Figure 2.5. Circuit design and information of microchips for the wearable power transmitter	45
Figure 2.6. Wireless coupling by voltage induction to SMDDI	50
Figure 2.7. Drug release from SMDDI	53

Figure 2.8. Fabrication process of the backside of SMDDI.....	54
--	----

Chapter 3

Figure 3.1. Schematic illustrations of a multifunctional endoscope system.....	61
Figure 3.2. Representative images of a multifunctional endoscope system.....	62
Figure 3.3. Composition of the graphene-hybrid.....	70
Figure 3.4. Characterizations of the graphene-hybrid.....	71
Figure 3.5. Graphene-hybrid based tumor and pH sensor.....	72
Figure 3.6. Graphene-hybrid based RF ablation electrode.....	73
Figure 3.7. Graphene-hybrid based temperature and contact sensor.....	74
Figure 3.8. Graphene-hybrid based viability sensor.....	75

Chapter 4

Figure 4.1. Localized delivery of theranostic NPs and high-energy photons for brain tumor treatment.....	88
Figure 4.2. Fabrication, design, and characterization of BMNs.....	91
Figure 4.3. Fluorescence measurement setup and focusing position.....	92
Figure 4.4. Characterization of LMNs.....	95
Figure 4.5. Simulation model and results for the light scattering by the alumina MP embedded in the LMNs.....	96
Figure 4.6. Calculated 3D visualization of the light distribution depending on the LMN length.....	97
Figure 4.7. Characterization of LMN-integrated bioelectronics.....	100

Figure 4.8. Optical camera images of the bioelectronics.....	101
Figure 4.9. Step-by-step fabrication and integration process of the bioelectronics.....	102
Figure 4.10. Characterizations of the temperature monitoring by the bioelectronics.....	103

List of Tables

Chapter 1

Table 1.1. Comparison of functional applications of nanomaterials and their performances.....	6
--	---

Chapter 1. Recent advances in wearable, implantable, and minimally-invasive bioelectronics using functional nanomaterials

1.1 Introduction

Substantial efforts have been devoted to solving many clinical challenges by means of flexible and stretchable electronics. This has led to the emergence of a unique field known as soft bioelectronics. The primary purpose of soft bioelectronics is the collection of clinically important biosignals such as physiological^{1,2}, electrophysiological^{3,4}, electrochemical^{5,6}, and mechanical signals^{7,8} with high signal-to-noise ratio and fidelity. The delivery of feedback therapy is another important goal of soft bioelectronics. The system consists of multifunctional sensors^{6,7,9}, active electronics¹⁰⁻¹², data storage modules¹³⁻¹⁵, energy storage elements^{16,17}, which are used to collect, store, and process relevant biosignals to trigger the appropriate therapy on the diseased site by using various drug/therapeutic actuators¹⁸⁻²⁰. To maximize the signal quality and device conformability, as well as minimize unpleasant mechanical loadings, immune responses, and the occurrence of inflammations^{21,22}, it is necessary for the mechanical properties of the applied devices to match those of the soft and curvilinear tissues in the human body. Consequently, a new device platform which is mechanically more compliant than conventional rigid and bulky

electronics but shows high performances comparable to them is highly required for soft bioelectronics.

In this review, we introduce individual devices and representative integrated systems of soft bioelectronics. Of particular interest are soft systems which incorporate functional nanomaterials that afford high performance²³⁻²⁶, unconventional biomedical functions²⁷⁻²⁹, mechanical advantages³⁰, and effective encapsulations^{31,32} for sensing³³⁻³⁵, energy storage³⁶⁻³⁸, and feedback treatment^{12,39} in wearable, implantable, and minimally-invasive applications⁴⁰⁻⁴². We first present functional units that can be derived from zero, one, and two dimensional (0D, 1D, and 2D) nanomaterials or their combinations. And we introduce representative devices composed of those functional building blocks and their target organs/tissues in or on the human body. Subsequently, we introduce examples of the individual devices such as soft biosensors, logic transistors, memory devices, light emitting diodes with skin-mounted configurations, and then describe implantable systems comprised of signal sensing, amplifying, data storage, and wireless transmission elements. Also, we present some minimally-invasive systems composed of functional nanomaterials. The review is finally concluded with a brief comment on the future prospects of soft medical electronics and personalized healthcare devices.

1.2 Nanomaterials as a functional basis of soft bioelectronics

Soft bioelectronic systems in wearable, implantable, and minimally-invasive format show extraordinary performances and novel functions derived from functional nanomaterials. Although there are numerous types of soft bioelectronic devices, the key nanomaterials and their unique functions can be classified into few groups. It is important to know what types of functional units are utilized and how they function as building blocks of the soft bioelectronic devices. Figure 1.1 shows representative images of 0D, 1D, and 2D nanomaterials and corresponding functions of their derivatives for specific soft bioelectronic systems. We have shown two examples of functional roles for each dimensional nanomaterials. First, 0D nanomaterials⁴³ can provide functions of light emission and charge transport control to soft bio-integrated electronic devices (red). Carefully designed quantum dots (QD) can emit light of various wavelength depending on their nanoscale size, thus providing controllable light emitting functions to bioelectronic devices⁴³. Metal nanoparticles that have appropriate work function can provide charge trapping sites, by which the charge trap layer for information storage¹⁴ or low power consumption³⁹ can be achieved. In case of 1D nanomaterials⁴⁴, piezoelectricity⁴⁵ and high level of conductivity with superb mechanical deformability¹¹ are widely utilized for self-power-supplying sensors and deformable electrodes, respectively (green). Aligned poly(vinylidene fluoride) (PVDF) nanofibers provide electricity generation function which is triggered

by applied pressure⁴⁵. Ligand-exchanged silver nanowire (Ag NW) could form a deformable heater which maintains its heating performance during 60% stretching¹¹. Recently emerging 2D nanomaterials⁴⁶ having superb photoresponsivity and semiconducting properties attract enormous attentions because they are promising candidates for substitution of current rigid and thick silicon-based electronics (blue). Ultrasensitive photodetectors could be fabricated by using a single layer of molybdenum disulphide (MoS₂)⁴⁷ and deformable charge trap memory array could be fabricated by using silicon nanoribbons (Si NR)¹⁴.

Some functional units can be formed using one or more types of nanomaterials (black). For example, both 0D and 1D nanomaterials such as metal nanoparticles and nanowires can be utilized to construct piezoresistive conductor. In case of transparent conductors, both metal nanowires (1D) and graphene (2D) can be considered as the source materials. To increase the surface to volume ratio for effective chemical reaction, oxide nanoparticles (0D)⁴⁸ and graphene (2D)⁶ are widely utilized in various chemical reaction applications. The aforementioned functional units construct the key functions of the soft bioelectronic devices which we are going to discuss. Therefore, the strategies of integrating one or more functional units with the soft bioelectronics are important to apply those in biomedical purposes. The functions and performances of various nanomaterials utilized in the soft bioelectronics are briefly described in Table 1.1

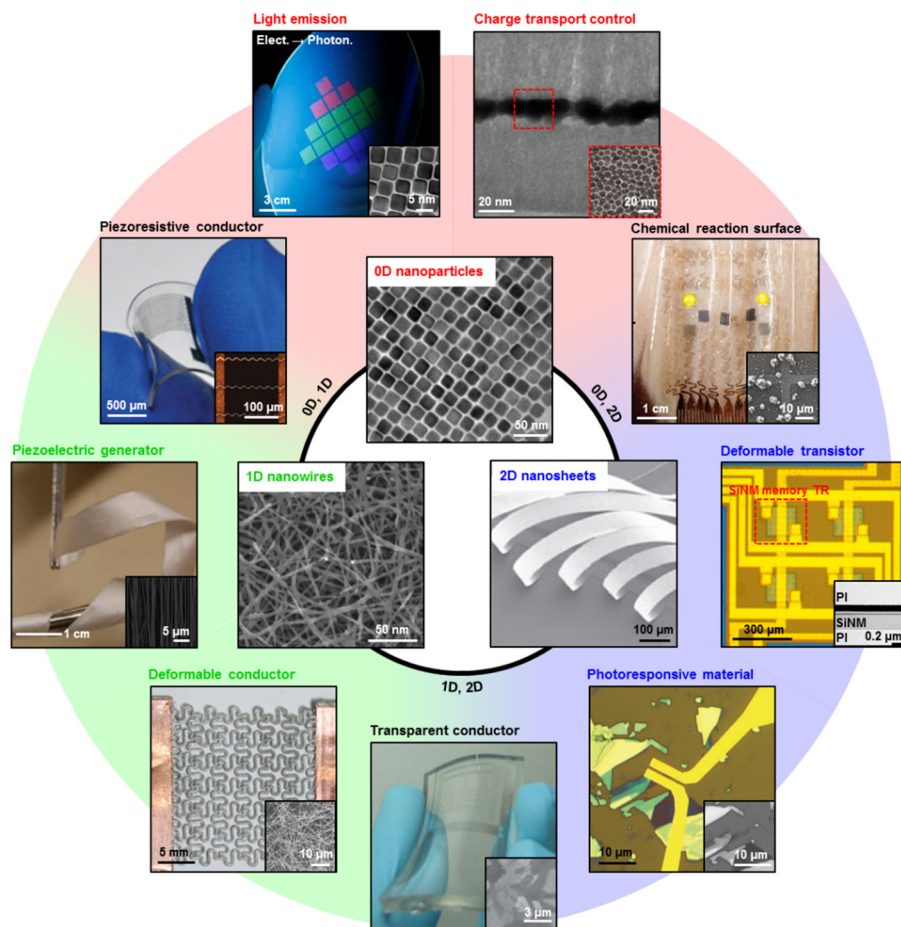


Figure 1.1. Soft nanomaterials and functional applications for bioelectronics⁷⁶. 0D, 1D, and 2D nanomaterials are utilized to provide various functions in single or hybrid format.^{6,11,14,39,43–47,49,50}

	Nanomaterials	Characteristics	Performances
Charge transport control	Au NP ^{14,39} Ag NP ⁵¹	Charge isolation ^{14,39} Carrier doping ⁵¹	Memory window ~15 V (for Au NP floating gate for -20~20 V sweep), ~11 V (for Au film floating gate for same condition) ¹⁴ Current limiting < 10% operation current compared to ReRAM without Au NP ³⁹
Electrodes	Graphene ⁴⁹ Ag NW ^{11,52} Au NW ⁵³	High conductivity ^{11,52,53} Transparency ^{49,54} Deformability ^{11,52,53}	Sheet resistance 30 Ω/sq (for doped graphene of 90% transparency at 550 nm) ⁵⁵ , 10 Ω/sq (for Ag NW of >90% transparency at 550 nm) ⁵⁶
Energy conversion	QD ⁴³ UCNP ⁵⁷	Efficient light emission ^{43,57}	Efficiency ~10 ⁻² W/W (for UCNP with excitation intensity 100 W/cm ²) ⁵⁸ , 14.5% (for green QLED) ⁵⁹ , 12.0% (for red QLED) ⁵⁹ , 10.7% (for blue QLED) ⁵⁹
Piezoresponsivity	Au NP ⁶⁰ Pt NW ⁶¹ PVDF NF ⁴⁵	Piezoresistivity ^{60,61} Piezoelectricity ⁴⁵	Sensitivity 11.45 (gauge factor for Pt nano-interlocked sensor, up to 10000 cycles) ⁶¹ 1.1V kPa ⁻¹ (for PVDF nanofiber response to external pressure) ⁴⁵
Deformable semiconductor	Si NR ^{7,14} CNT ¹³ MoS ₂ ⁶²	Single crystalline ^{7,14,62} High carrier mobility ^{7,14,62} Deformability ¹³	Mobility (cm ² /V*s) ~270 (for Si NR) ⁶³ , ~400 (for strained Si NR) ⁶³ , ~50 (for CNT network) ⁶⁴ , ~30 (for MoS ₂ FET) ⁶⁵

Table 1.1. Comparison of functional applications of nanomaterials and their performances⁷⁶.

1.3 Soft bio-integrated electronics based on functional nanomaterials

Figure 1.2 shows representative examples of the soft bio-integrated systems. The basic nanomaterials with novel functions mentioned above are elaborately integrated to develop soft bioelectronic devices for specific purposes. These bio-integrated electronic systems can generally be classified into three categories, namely, wearable (skin-mounted), implantable, and minimally-invasive systems. Although the systems are usually developed using similar classes of flexible/stretchable sensors and electronics, the imposed constraints vary within the intended purpose. For example, skin-mounted wearable electronics require highly flexible/stretchable features owing to the soft nature of the skin^{4,43}. Conversely, highly conductive materials and high-quality encapsulation materials are required in implantable systems that monitor the electrophysiological signals emanating from internal organs^{3,52,66}. Meanwhile, miniaturization and optical transparency are required in supplemental devices mounted on minimally-invasive systems such as conventional endoscopes⁵⁴. Obviously, some properties such as material biocompatibility and device reliability are required in all types of systems. Different bio-integrated systems thus require different types of functional nanomaterials with specific characteristics, and the employed device design strategy depends on the details of the intended application. In the following sections, we review the recent studies on soft bioelectronics equipped with functional nanomaterials, employed in biomedical applications of wearable, implantable, and minimally-invasive forms.

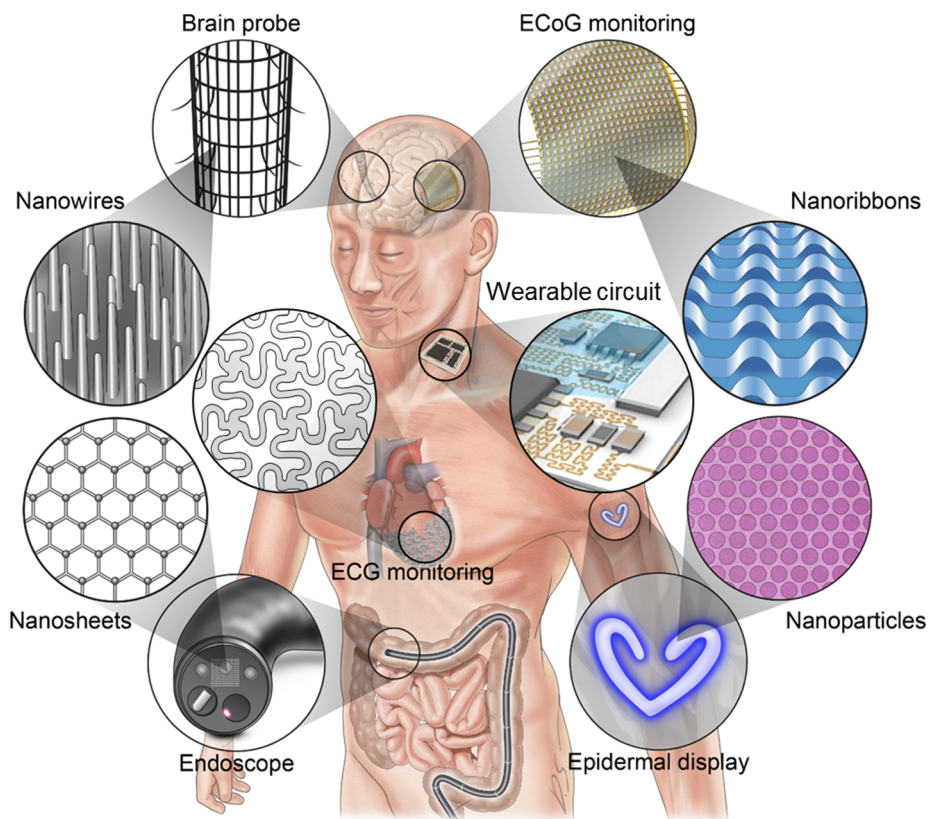


Figure 1.2. Schematic illustration of wearable, implantable, and minimally-invasive devices incorporating functional nanomaterials⁷⁶. The soft bioelectronic systems include an epidermal display equipped with quantum dot NPs, silicon NW/NR-ribbon-based electrophysiological sensors (ECoG, ECG), and a smart endoscope for colon cancer diagnosis/therapy using graphene nanosheets. ^{3,4,43,52,54,66}

1.4 Wearable systems using soft bioelectronics

Wearable electronic devices available in the market are mostly accessory types, which can be worn in the form of watches or clothes, and made by using conventional rigid components. However, these wearable devices have many limitations for healthcare applications. This is because they are mechanically rigid, uncomfortable, incapable of measuring subtle physiological or electrophysiological changes with high reliability, and cannot deliver drugs for point-of-care therapy. Recent studies on wearable electronics have thus focused on developing flexible and stretchable devices which can be intimately laminated onto the human body. The incorporation of high quality nanomaterials in wearable systems enabled unique device performances.

The left image in Fig. 1.3a shows a recently reported wearable charge trap floating gate memory (CTFM) that uses silicon nanoribbons (Si NRs) as the active materials of the field-effect transistors, and gold nanoparticles (Au NPs) for the charge trap layer¹⁴. The Au NPs were directly assembled by the Langmuir-Blodgett (LB) method (Fig. 1.3a, right) as a monolayer on the stretchable Si NR devices. The Au NPs layer as a floating gate of CTFM can effectively trap and isolate the injected charges because of the ligands covering the Au NPs. Therefore, the heterogeneous integration afforded a long retention time and large memory window of the CTFM. Multiple layers of the Au NPs assembled by LB method can also be used in a wearable resistive random access memory (ReRAM). The integrated NPs effectively trap carriers during operation of ReRAM, thereby reducing the current and power consumption.

This is an important advancement because low energy consumption is highly required for wearable applications which are operated using limited power sources. Figure 3b shows an ReRAM array conformally laminated on the human skin (left), and a cross-sectional transmission electron microscope (TEM) image of the embedded Au NPs in a memory pixel (right)³⁹.

There are other nanomaterials which can be used in wearable devices. For example, Park and collaborators incorporated carbon nanotubes (CNTs) and silver nanoparticles (Ag NPs) in a wearable transparent device fabricated from ZnO thin films for monitoring human motion and body temperature⁵¹. The device was used to control a wheelchair and alert sudden body temperature changes (Fig. 1.3c, left). CNT networks having native p-type characteristics were deposited on a piezoelectric ZnO layer to neutralize the native surface defects of the n-type ZnO film. This dramatically amplified the piezoelectric signals of the motion sensor. The Ag NPs were incorporated in between the Al₂O₃-doped ZnO layers to increase the carrier doping intensity and consequently increase the sensitivity of the temperature sensor (Fig. 1.3c, right). Light-emitting nanomaterials such as quantum dots are also useful for fabricating an ultrathin wearable display that can potentially be utilized to indicate helpful information on human skin (Fig. 1.3d, left)⁴³. Choi and collaborators reported wearable quantum-dot light-emitting diodes (QDLEDs) with a total thickness of only 2.6 μm (Fig. 1.3d, right), which enabled conformal integration on the skin. The emission color of the wearable QDLEDs could be easily tuned by modifying the quantum dot size, and high-resolution patterning

for full color display could be achieved by the novel intaglio transfer printing technology.

Electronic skin is another example of the soft bioelectronic devices. Kim and collaborators reported a Si NR-based skin-like sensor array (Fig. 1.3e, left)⁷. This prosthetic skin is multifunctional, capable of sensing pressure, strain, temperature, and humidity, as well as functioning as an embedded heater to emulate the skin temperature. A cavity was deliberately formed beneath the Si NR pressure sensor to enhance the sensitivity (Fig. 1.3e, right). Then the authors stimulated peripheral nerves with electrical signals measured by the prosthetic skin and simultaneously read the signals delivered to brain. This demonstrates the potentials that a prosthetic skin can directly measure the external stimuli and deliver them to somatosensory part of brain to realize a skin-like sense. While this electronic skin utilizes a direct current (DC) stimulation of peripheral nerves to transfer the external stimuli, a recently reported artificial mechanoreceptor system uses an alternating current (AC) modulation and optical stimulation (Fig. 1.3f, left), which is more realistic⁸. To achieve a wide dynamic sensing range of the pressure sensor which is comparable to typical pressure range of grip control, CNT composites were dispersed in an elastomer molded into a pyramidal microstructure (Fig. 1.3f, right). The monitored signals were converted into optical oscillating pulses and directly injected into a transgenic sensory cortex for their transmission to the central nervous system.

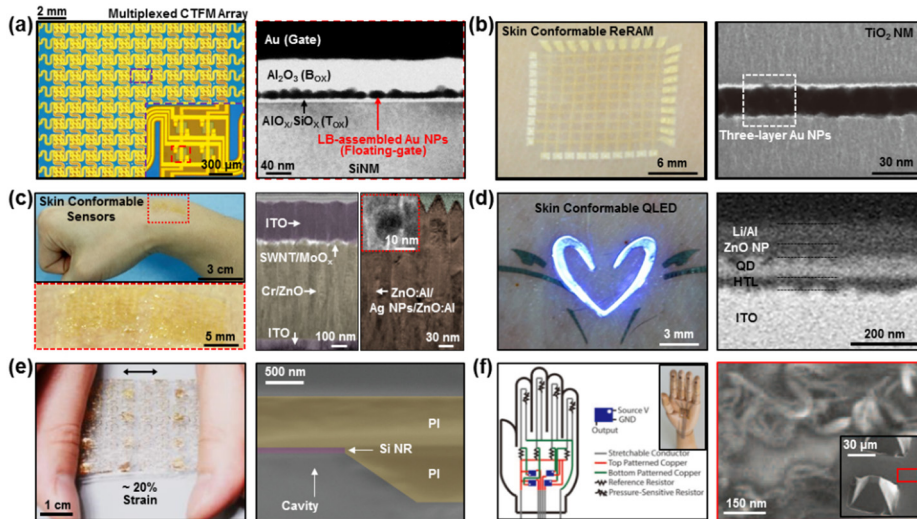


Figure 1.3. Wearable bioelectronics⁷⁶. **(a)** An optical image of a wearable CTFM array (left), an enlarged view showing four memory pixels (inset), and a cross-sectional TEM image of the CTFM's channel area (right)¹⁴. **(b)** An optical image of a skin-conformable ReRAM array (left), and a cross-sectional TEM image of an ReRAM pixel showing the Au NP layers (right)³⁹. **(c)** An optical image of a wearable sensor (left), and a colored cross-sectional TEM image of the sensors incorporating CNT networks and Ag NPs (right). Inset is a magnified view of a Ag NP⁶⁷. **(d)** An optical image of a skin-conformable quantum dot display which emits blue color (left), and a cross-sectional TEM image of its detailed structure (right)⁴³. **(e)** An optical image of a stretched electronic skin incorporating Si NR-based mechanical sensors (left), and a cross-sectional colored SEM image of the pressure sensor showing a deliberately formed cavity (right)⁷. **(f)** A schematic illustration of an artificial mechanoreceptor system incorporating pressure sensors and organic transistor circuits (left), and an optical image of the actual mechanoreceptor system (inset on the left frame), and a magnified SEM image showing a CNT-elastomer composite (right) with pyramidal micro-structures (inset in the right panel)⁸.

1.5 Implantable devices based on soft bioelectronics

Implantable devices are different from skin-mounted wearable systems in that they are highly invasive and require surgery. But they are more useful for collecting high-quality electrophysiological and/or physiological signals from important organs compared to the wearable type devices. Figure 1.4a shows a Si NR-based electrocorticogram (ECoG) sensor array, which is used to monitor brain activity with high spatial and temporal resolution³. Such a multichannel ECoG sensor array enables high-precision surgical removal of a seizure focus. The possibility of using the sensor to diagnose micro-seizures was verified by monitoring the spiral waves which originate from the visual cortex of a feline model (Fig. 1.4a, right). Figure 1.4b left shows a Si NR-based multifunctional cardiac implant composed of the ECG sensor and strain, pH, and temperature sensors⁶⁸. The multifunctional system is conformally wrapped around the epicardium and has been found to be capable of distinguishing different states of a diseased heart (Fig. 1.4b right).

Transient electronic systems have emerged as novel implantable devices, enabling the avoidance of post-surgery procedure to remove the expired implants. They are composed of bio-resorbable materials such as magnesium, silicon, magnesium oxide, and silk, which are naturally dissolved and resorbed within the body. Figure 1.4c shows a logic circuit which utilizes such bio-resorbable materials⁶⁹. The circuit composed of a resistor, capacitor, inductor, diode, and transistor is demonstrated with transiently reducing resonance responses during dissolution and heating for thermal therapy, *in vivo*. Son and collaborators presented a different example in which physiological

signals were collected by a bio-resorbable stent implanted by an angioplasty procedure⁷⁰. The bio-resorbable electronic stent was equipped with a flow sensor for monitoring the blood flow, and a non-volatile memory device for data storage (Fig. 1.4d). The integration of biocompatible nanomaterials in the stent would facilitate the scavenging for reactive oxygen species using ceria NPs and controlled drug delivery using mesoporous silica and Au nanorods. The authors also showed potentials that collected signals including the blood flow speed and temperature can be stored and wirelessly transferred to signal analysing equipment.

Other types of implantable systems particularly designed for therapeutic functions have also been reported. Figure 1.4e shows a cell culture platform which enhances tissue regeneration through aligned cell sheets fabricated on a patterned graphene¹⁹. The cultured cells are aligned with the graphene patterns to get appropriate physiology. Then the induced cell physiology during proliferation and differentiation is monitored by embedded stretchable Au NR sensors. Figure 1.4f shows another fully implantable, wireless optogenetic actuation device⁷¹. Optogenetics typically employs long optical guiding wires connected to a light source, and this places substantial constraints on the movement of the subject. During a mice experiment, this physical limitation was overcome by an implantable light emitting system integrated with soft radiofrequency wireless module (Fig. 1.4f, left), which enabled wireless modulation of the pain circuit in the spinal cord of the animal (Fig. 4f, right).

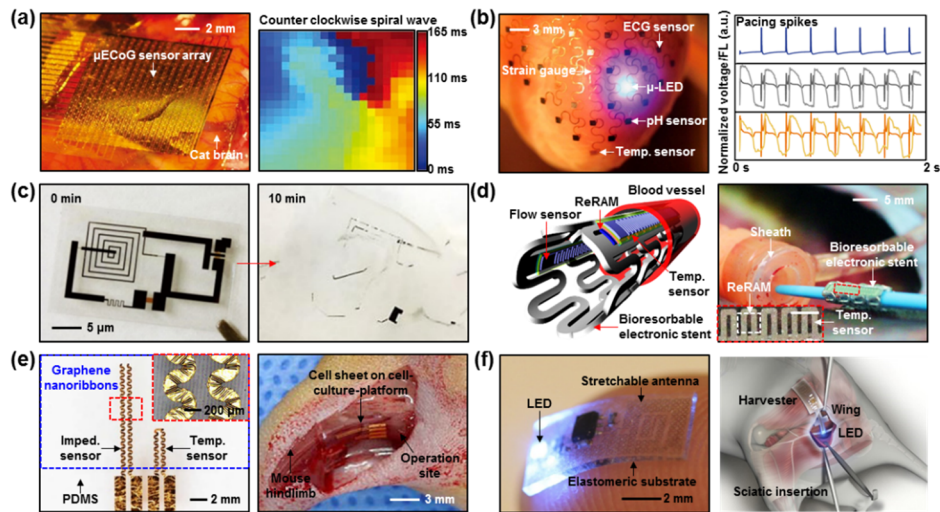


Figure 1.4. Implantable devices⁷⁶. **(a)** An optical image of a flexible and multiplexed electrode array on the visual cortex of a cat brain (left), and a high-density map of a counter-clockwise spiral wave of a cat (right)³. **(b)** An optical image of a 3D multifunctional integumentary mesh including an ECG sensor, strain sensor, pH sensor, temperature sensor, and μ -LED (left); and the ECG responses to pacing spikes (right)⁶⁸. **(c)** Images of the time-dependent dissolution of transient electronics before and after exposure to water⁶⁹. **(d)** Schematic illustration (left) and image of a surgical procedure using (right) a bio-resorbable stent incorporating electrophysiological sensors, non-volatile memories, and therapeutic NPs⁷⁰. **(e)** A stretchable cell culture platform based on graphene NRs and ceria NPs¹⁹. **(f)** An optical image of a miniaturized stretchable optoelectronic device with a wireless control unit (left), and a schematic illustration of an optogenetic device implanted in a mice (right)⁷¹.

1.6 Minimally-invasive surgical tools based on soft bioelectronics

Minimally-invasive surgical tools have been extensively investigated over the last few years to minimize the tissue damage caused by conventional surgical procedures, and to shorten the post-surgery recovery time. Some representative examples include electronic balloon catheters for dealing with cardiovascular diseases and arrhythmias; advanced endoscopes for gastrointestinal, stomachic, and brain surgeries; and highly precise robotic surgical tools. Considerable progress has been achieved along this line through the integration of nanomaterial-based multifunctional sensors and actuators for minimally-invasive surgery. For example, an array of ECG, tactile, temperature, and flow sensors with ablation electrodes was integrated in a balloon catheter for accurate diagnosis and treatment of arrhythmias (Fig. 1.5a, left) and ischemia, tachycardia, and fibrillation through feedback radiofrequency ablation therapy (Fig. 1.5a, right)⁷².

Figure 1.5b shows another example, a surgical endoscope equipped with transparent electronics and theranostic NPs for the diagnosis and treatment of colon cancers⁵⁴. Graphene and Ag NWs are used as transparent conductors, electrochemical tumor detectors, and pH sensors. The co-integration of theranostic NPs containing Au nanorods, drug-loaded silica nanoshells, chlorin e6 dye, and antibodies has been used for photothermal therapy, chemo-therapy, photodynamic therapy, and active tumor targeting, respectively. *In vivo* studies have also demonstrated that the device can be effectively used to diagnose and

remove colon cancer tissues without hindering the original endoscopic functions (Fig. 1.5b, right).

There have been recent reports of other unconventional surgical tools which utilize novel materials and design concepts. Canales and collaborators reported a multifunctional fiber which can be used for neural recording, optical stimulation, and drug delivery (Fig. 1.5c, left)⁷³. This multifunctional fiber was fabricated by thermal drawing process, which enables the integration of various functional structures to realize the multifunctional fiber and maintain functionalities during bending deformation. Owing to the integrated functional structures in a fiber of minimized footprint, various *in vivo* procedures such as optogenetical stimulation, neural recordings, and drug delivery could be successfully conducted within a single implantable platform (Fig. 1.5c, right). Upgraded version of fibers integrated with nanomaterials for recording and stimulation of spinal cord are recently reported. Lu and collaborators developed stretchable fibers for optoelectronic probing of spinal cord by thermal drawing process combined with Ag NW dip coating. (Fig. 1.5d, left)⁷⁴. Because neural probing devices should be soft enough to match the modulus of neural tissue, a highly flexible and stretchable fiber is suitable for spinal cord implantation. In addition, this Ag NW-coated hybrid fiber is transparent and has low impedance, enabling optoelectronic stimulation and recording neural responses simultaneously (Fig. 1.5d, right).

In another study, Xie and collaborators demonstrated a mesh-type neural recording and stimulation device which utilizes ultra-flexible Si NW-

based nanoelectronic probes (Fig. 1.5e, left)⁶⁶. These macroporous brain probes can be directly injected to brain and record neural signals through multichannel electrodes. Because the probes are ultrathin and have macroporous structures, brain tissue could be effectively regenerated from the damage caused during probe insertion to the brain tissue (Fig. 1.5e, right). A similar device but with a different implantation method has also been reported. In the demonstration of this device, a mesh-shaped multichannel electrode array which uses Si NWs and ultrathin Au mesh electrodes was injected into a mouse brain through a syringe (Fig. 1.5f, left)⁷⁵. This syringe-injectable nanoelectronics can be used to record neural signals within small cavities in the brain with minimal invasiveness (Fig. 1.5f, right).

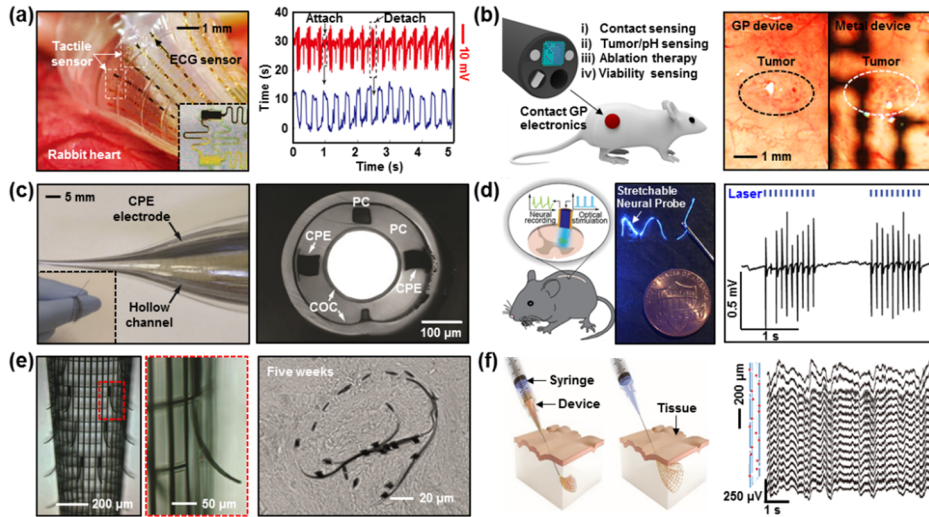


Figure 1.5. Minimally-invasive devices⁷⁶. **(a)** An optical image of a multifunctional balloon catheter with an ECG sensor, a tactile sensor, a temperature sensor, a flow sensor, and ablation electrodes (left). The device was used to measure the ECG signals at an epicardiac interface in a rabbit heart (right)⁷². **(b)** A schematic illustration of an instrumented smart endoscope for the diagnosis/treatment of colon cancer (left), and optical images obtained by an endoscope camera with a transparent graphene device and metal device (right)⁵⁴. **(c)** An optical image of a fiber-based implantable optoelectronic system for wireless optogenetics and drug delivery (left), and a TEM image showing a cross section of the smart fiber (right)⁷³. **(d)** Optical images of stretchable neural probes (left) and simultaneous recording of neural signals during optoelectronics (right)⁷⁴. **(e)** Optical images of macroporous nanoelectronic network (left). The brain tissue damaged by the insertion of the device recovers after five weeks (right)⁶⁶. **(f)** A schematic illustration of the syringe injection of an electronic device (left), and a multichannel map of the signal from a mice brain injected with the mesh electronic device (right)⁷⁵.

1.7 Conclusion

Over the last few years, innovations in soft bioelectronics have been promoted by improvements in the fabrication and synthesis of nanomaterials and their integration with devices. Efforts have particularly been made to employ novel functional nanomaterials in soft devices for enhanced deformability, biocompatibility, multifunctionality, and overall performance. Nevertheless, there are still several challenges and opportunities in the field of nanomaterial-based soft bioelectronics. For instance, the long-term biocompatibility, stability, and reliability of the systems require careful investigations. Extensive studies on the manipulation of the nanomaterials to realize target-specific functions would also afford unprecedented advantages in personalized healthcare applications. We anticipate that continuous research and development of soft bioelectronics would open up huge opportunities in clinical medicine.

References

1. Webb, R. C. *et al.* Ultrathin conformal devices for precise and continuous thermal characterization of human skin. *Nat. Mater.* **12**, 938–944 (2013).
2. Webb, R. C. *et al.* Epidermal devices for noninvasive, precise, and continuous mapping of macrovascular and microvascular blood flow. *Sci. Adv.* **1**, e1500701–e1500701 (2015).
3. Viventi, J. *et al.* Flexible, foldable, actively multiplexed, high-density electrode array for mapping brain activity in vivo. *Nat. Neurosci.* **14**, 1599–1605 (2011).
4. Xu, S. *et al.* Soft Microfluidic Assemblies of Sensors, Circuits, and Radios for the Skin. *Science (80-.)*. **344**, 70–74 (2014).
5. Gao, W. *et al.* Fully integrated wearable sensor arrays for multiplexed in situ perspiration analysis. *Nature* **529**, 509–514 (2016).
6. Lee, H. *et al.* A graphene-based electrochemical device with thermoresponsive microneedles for diabetes monitoring and therapy. *Nat. Nanotechnol.* **11**, 566–572 (2016).
7. Kim, J. *et al.* Stretchable silicon nanoribbon electronics for skin prosthesis. *Nat. Commun.* **5**, 5747 (2014).
8. Tee, B. C.-K. *et al.* A skin-inspired organic digital mechanoreceptor. *Science (80-.)*. **350**, 313–316 (2015).
9. Song, J.-K. *et al.* Wearable Force Touch Sensor Array Using a Flexible and Transparent Electrode. *Adv. Funct. Mater.* **27**, 1605286 (2017).

10. Jung, S. *et al.* Reverse-Micelle-Induced Porous Pressure-Sensitive Rubber for Wearable Human-Machine Interfaces. *Adv. Mater.* **26**, 4825–4830 (2014).
11. Choi, S. *et al.* Stretchable Heater Using Ligand-Exchanged Silver Nanowire Nanocomposite for Wearable Articular Thermotherapy. *ACS Nano* **9**, 6626–6633 (2015).
12. Lee, H. *et al.* Wearable/disposable sweat-based glucose monitoring device with multistage transdermal drug delivery module. *Sci. Adv.* **3**, e1601314 (2017).
13. Son, D. *et al.* Stretchable Carbon Nanotube Charge-Trap Floating-Gate Memory and Logic Devices for Wearable Electronics. *ACS Nano* **9**, 5585–5593 (2015).
14. Kim, J. *et al.* A wearable multiplexed silicon nonvolatile memory array using nanocrystal charge confinement. *Sci. Adv.* **2**, e1501101–e1501101 (2016).
15. Son, D. *et al.* Colloidal Synthesis of Uniform-Sized Molybdenum Disulfide Nanosheets for Wafer-Scale Flexible Nonvolatile Memory. *Adv. Mater.* **28**, 9326–9332 (2016).
16. Jung, S., Lee, J., Hyeon, T., Lee, M. & Kim, D.-H. Fabric-Based Integrated Energy Devices for Wearable Activity Monitors. *Adv. Mater.* **26**, 6329–6334 (2014).
17. Jung, S. *et al.* Wearable Fall Detector using Integrated Sensors and Energy Devices. *Sci. Rep.* **5**, 17081 (2015).

18. Choi, M. K. *et al.* Cephalopod-Inspired Miniaturized Suction Cups for Smart Medical Skin. *Adv. Healthc. Mater.* **5**, 80–87 (2016).
19. Kim, S. J. *et al.* Multifunctional Cell-Culture Platform for Aligned Cell Sheet Monitoring, Transfer Printing, and Therapy. *ACS Nano* **9**, 2677–2688 (2015).
20. Kim, S. J. *et al.* Stretchable and Transparent Biointerface Using Cell-Sheet-Graphene Hybrid for Electrophysiology and Therapy of Skeletal Muscle. *Adv. Funct. Mater.* **26**, 3207–3217 (2016).
21. Jang, K.-I. *et al.* Soft network composite materials with deterministic and bio-inspired designs. *Nat. Commun.* **6**, 6566 (2015).
22. Norton, J. J. S. *et al.* Soft, curved electrode systems capable of integration on the auricle as a persistent brain–computer interface. *Proc. Natl. Acad. Sci.* **112**, 3920–3925 (2015).
23. Hwang, S. & Jeong, S.-H. Stretchable carbon nanotube conductors and their applications. *Korean J. Chem. Eng.* **33**, 2771–2787 (2016).
24. Prasanna, D. & Selvaraj, V. Pt and Pt-Sn nanoparticles decorated conductive polymer-biowaste ash composite for direct methanol fuel cell. *Korean J. Chem. Eng.* **33**, 1489–1499 (2016).
25. Kim, Y. Y., Hyun, W. J., Park, K. H., Ye, S. J. & Park, O. O. Synthesis of poly(3,4-ethylenedioxythiophene): poly(styrene sulfonate)-capped silver nanoparticles and their application to blue polymer light-emitting diodes. *Korean J. Chem. Eng.* **32**, 534–539 (2015).
26. Kim, H. C., Yoon, C., Song, Y.-G., Kim, Y.-J. & Lee, K. Enhancing

- performance of quantum dot-based light emitting diodes by using poly(methyl methacrylate)/quantum dot hybrid particles. *Korean J. Chem. Eng.* **32**, 563–566 (2015).
27. Kazemi, S., Sarabi, A. A. & Abdouss, M. Synthesis and characterization of magnetic molecularly imprinted polymer nanoparticles for controlled release of letrozole. *Korean J. Chem. Eng.* **33**, 3289–3297 (2016).
28. Dorraji, M. S. S., Ashjari, H. R., Rasoulifard, M. H. & Rastgouy-Houjaghan, M. Polyurethane foam-cadmium sulfide nanocomposite with open cell structure: Dye removal and antibacterial applications. *Korean J. Chem. Eng.* **34**, 547–554 (2017).
29. Fatima, H. & Kim, K.-S. Magnetic nanoparticles for bioseparation. *Korean J. Chem. Eng.* **34**, 589–599 (2017).
30. Kim, H. J. *et al.* Improving the tensile strength of carbon nanotube yarn via one-step double [2+1] cycloadditions. *Korean J. Chem. Eng.* **33**, 299–304 (2016).
31. Kim, S. W. & Choi, H. M. Morphology, thermal, mechanical, and barrier properties of graphene oxide/poly(lactic acid) nanocomposite films. *Korean J. Chem. Eng.* **33**, 330–336 (2016).
32. Lim, S. H., Seo, S.-W., Lee, H., Chae, H. & Cho, S. M. Extremely flexible organic-inorganic moisture barriers. *Korean J. Chem. Eng.* **33**, 1971–1976 (2016).
33. Choi, E. *et al.* Effect of chemical mechanical treatment on the optoelectronic properties in CMOS image sensor. *Korean J. Chem. Eng.*

- 32**, 199–201 (2015).
34. Kim, J., Oh, S. Y., Park, J. Y. & Kim, Y. Electrochemical sensor applications of Pt supported porous gold electrode prepared using cellulose-filter. *Korean J. Chem. Eng.* **33**, 344–349 (2016).
 35. Pham, Q. M. & Kim, S. High surface area polyaniline nanofiber synthesized in compressed CO₂ and its application to a hydrogen sensor. *Korean J. Chem. Eng.* **33**, 290–298 (2016).
 36. Park, H., Yeom, D. H., Kim, J. & Lee, J. K. MnO/C nanocomposite prepared by one-pot hydrothermal reaction for high performance lithium-ion battery anodes. *Korean J. Chem. Eng.* **32**, 178–183 (2015).
 37. Im, Y. *et al.* Electrochemical performance of three shaped ZnO nanoparticles prepared in LiOH, NaOH and KOH alkaline solutions as anodic materials for Ni/Zn redox batteries. *Korean J. Chem. Eng.* **33**, 1447–1455 (2016).
 38. Venugopal, N., Kim, W.-S. & Yu, T. A facile synthetic route for Co₃O₄ nanoparticle/porous carbon composite as an efficient anode material for lithium-ion batteries. *Korean J. Chem. Eng.* **33**, 1500–1504 (2016).
 39. Son, D. *et al.* Multifunctional wearable devices for diagnosis and therapy of movement disorders. *Nat. Nanotechnol.* **9**, 397–404 (2014).
 40. Yang, J., Choi, M. K., Kim, D.-H. & Hyeon, T. Designed Assembly and Integration of Colloidal Nanocrystals for Device Applications. *Adv. Mater.* **28**, 1176–1207 (2016).
 41. Choi, S., Lee, H., Ghaffari, R., Hyeon, T. & Kim, D.-H. Recent

- Advances in Flexible and Stretchable Bio-Electronic Devices Integrated with Nanomaterials. *Adv. Mater.* **28**, 4203–4218 (2016).
42. Kim, J., Ghaffari, R. & Kim, D.-H. The quest for miniaturized soft bioelectronic devices. *Nat. Biomed. Eng.* **1**, 0049 (2017).
 43. Choi, M. K. *et al.* Wearable red–green–blue quantum dot light-emitting diode array using high-resolution intaglio transfer printing. *Nat. Commun.* **6**, 7149 (2015).
 44. Lee, S. S. *et al.* A transparent bending-insensitive pressure sensor. *Nat. Nanotechnol.* **11**, 472–478 (2016).
 45. Persano, L. *et al.* High performance piezoelectric devices based on aligned arrays of nanofibers of poly(vinylidene fluoride-co-trifluoroethylene). *Nat. Commun.* **4**, 1633 (2013).
 46. Kim, D.-H., Lu, N., Huang, Y. & Rogers, J. A. Materials for stretchable electronics in bioinspired and biointegrated devices. *MRS Bull.* **37**, 226–235 (2012).
 47. Lopez-Sanchez, O., Lembke, D., Kayci, M., Radenovic, A. & Kis, A. Ultrasensitive photodetectors based on monolayer MoS₂. *Nat. Nanotechnol.* **8**, 497–501 (2013).
 48. Zheng, Z. Q., Yao, J. D., Wang, B. & Yang, G. W. Light-controlling, flexible and transparent ethanol gas sensor based on ZnO nanoparticles for wearable devices. *Sci. Rep.* **5**, 11070 (2015).
 49. Kim, K. S. *et al.* Large-scale pattern growth of graphene films for stretchable transparent electrodes. *Nature* **457**, 706–710 (2009).

50. Su, M. *et al.* Nanoparticle Based Curve Arrays for Multirecognition Flexible Electronics. *Adv. Mater.* **28**, 1369–1374 (2016).
51. Park, M. *et al.* Oxide Nanomembrane Hybrids with Enhanced Mechano- and Thermo-Sensitivity for Semitransparent Epidermal Electronics. *Adv. Healthc. Mater.* **4**, 992–997 (2015).
52. Park, J. *et al.* Electromechanical cardioplasty using a wrapped elasto-conductive epicardial mesh. *Sci. Transl. Med.* **8**, 344ra86-344ra86 (2016).
53. Gong, S. *et al.* A wearable and highly sensitive pressure sensor with ultrathin gold nanowires. *Nat. Commun.* **5**, 3132 (2014).
54. Lee, H. *et al.* An endoscope with integrated transparent bioelectronics and theranostic nanoparticles for colon cancer treatment. *Nat. Commun.* **6**, 10059 (2015).
55. Bae, S. *et al.* Roll-to-roll production of 30-inch graphene films for transparent electrodes. *Nat. Nanotechnol.* **5**, 574–578 (2010).
56. Krantz, J., Richter, M., Spallek, S., Spiecker, E. & Brabec, C. J. Solution-processed metallic nanowire electrodes as indium tin oxide replacement for thin-film solar cells. *Adv. Funct. Mater.* **21**, 4784–4787 (2011).
57. Lee, J. *et al.* Ultra-Wideband Multi-Dye-Sensitized Upconverting Nanoparticles for Information Security Application. *Adv. Mater.* **29**, 1603169 (2017).
58. Nadort, A. *et al.* Quantitative Imaging of Single Upconversion

- Nanoparticles in Biological Tissue. *PLoS One* **8**, (2013).
59. Yang, Y. *et al.* High-efficiency light-emitting devices based on quantum dots with tailored nanostructures. *Nat. Photonics* **9**, 1–9 (2015).
 60. Jiang, C., Ni, I.-C., Tzeng, S. & Kuo, W. Nearly isotropic piezoresistive response due to charge detour conduction in nanoparticle thin films. *Sci. Rep.* **5**, 11939 (2015).
 61. Pang, C. *et al.* A flexible and highly sensitive strain-gauge sensor using reversible interlocking of nanofibres. *Nat. Mater.* **11**, 795–801 (2012).
 62. Yu, W. J. *et al.* Highly efficient gate-tunable photocurrent generation in vertical heterostructures of layered materials. *Nat. Nanotechnol.* **8**, 952–958 (2013).
 63. Zhou, H. *et al.* Fast flexible electronics with strained silicon nanomembranes. *Sci. Rep.* **3**, 1291 (2013).
 64. Cai, L. & Wang, C. Carbon Nanotube Flexible and Stretchable Electronics. *Nanoscale Res. Lett.* **10**, 320 (2015).
 65. Chang, H. Y. *et al.* High-performance, highly bendable MoS₂ transistors with high-K dielectrics for flexible low-power systems. *ACS Nano* **7**, 5446–5452 (2013).
 66. Xie, C. *et al.* Three-dimensional macroporous nanoelectronic networks as minimally invasive brain probes. *Nat. Mater.* **14**, 1286–1292 (2015).
 67. Lim, S. *et al.* Transparent and Stretchable Interactive Human Machine Interface Based on Patterned Graphene Heterostructures. *Adv. Funct. Mater.* **25**, 375–383 (2015).

68. Xu, L. *et al.* 3D multifunctional integumentary membranes for spatiotemporal cardiac measurements and stimulation across the entire epicardium. *Nat. Commun.* **5**, 3329 (2014).
69. Hwang, S.-W. *et al.* A Physically Transient Form of Silicon Electronics. *Science (80-.)*. **337**, 1640–1644 (2012).
70. Son, D. *et al.* Bioresorbable Electronic Stent Integrated with Therapeutic Nanoparticles for Endovascular Diseases. *ACS Nano* **9**, 5937–5946 (2015).
71. Park, S. I. *et al.* Soft, stretchable, fully implantable miniaturized optoelectronic systems for wireless optogenetics. *Nat. Biotechnol.* **33**, 1280–1286 (2015).
72. Kim, D.-H. *et al.* Materials for multifunctional balloon catheters with capabilities in cardiac electrophysiological mapping and ablation therapy. *Nat. Mater.* **10**, 316–323 (2011).
73. Canales, A. *et al.* Multifunctional fibers for simultaneous optical, electrical and chemical interrogation of neural circuits in vivo. *Nat. Biotechnol.* **33**, 277–284 (2015).
74. Lu, C. *et al.* Flexible and stretchable nanowire-coated fibers for optoelectronic probing of spinal cord circuits. *Sci. Adv.* **3**, e1600955 (2017).
75. Liu, J. *et al.* Syringe-injectable electronics. *Nat. Nanotechnol.* **10**, 629–636 (2015).
76. Lee, Y. *et al.* Nanomaterials for bioelectronics and integrated medical

systems. *Korean J. Chem. Eng.* **35**, 1-11 (2018).

***Some contents of this chapter are published in *The Korean Journal of Chemical Engineering* (2017,35, 1).**

Thesis overview

In the Ph. D. course, I focused on developing implantable and minimally-invasive drug delivery system using soft bioelectronics. First, as described in consequent chapters, I built a soft miniaturized drug delivery implant (SMDDI) wirelessly integrated with wearables for treating status epilepticus (SE). Seizure is one of the most serious disease occurring in brain tissue. SE in which continuous seizure lasts longer than 5 min requires urgent treatment. Without an immediate treatment, significant side effect such as brain damage can occur and mortality can be low. Therefore, I developed SMDDI which is wirelessly integrated with wearables to monitor electroencephalography and deliver drug for diagnosis and treatment of SE.

Second, I developed a smart endoscope system integrated with soft bioelectronics and theranostic nanoparticles (NPs) for colon cancer treatment. Colon cancer is usually diagnosed and treated by surgical endoscope. However, diagnosis and treatment of colon cancer are separated protocol and request long time. Therefore, I developed smart endoscope system which can precisely diagnose and treat colon cancer, simultaneously.

Different from other organs, drug delivery for brain cancer is significantly limited due to blood-brain barrier (BBB). The BBB is an essential barrier in a brain tissue, which also blocks the theranostic NPs. Therefore, I developed localized drug delivery system using microneedle-integrated bioelectronics. The localized delivery system can effectively treat brain tumors while avoiding unintended side effects on nearby normal tissues with minimal invasiveness.

Chapter 2. Soft miniaturized drug delivery implant wirelessly powered and controlled by wearables

2.1 Introduction

Wearable and implantable biomedical devices have emerged as key components for the closed-loop personalized healthcare platform¹⁻⁴. By combining devices for point-of-care therapy with biosensors that continuously monitor key health signals, real-time health monitoring and precisely controlled in-situ treatment can be achieved. For example, wearable devices providing sensing data to control transdermal drug delivery have been proposed⁵⁻⁸. The implantable pacemaker and/or defibrillator have provided programmed electrical stimulations based on the electrocardiogram measurement⁹⁻¹¹. Implantable drug delivery devices, such as insulin pumps, have customized drug delivery dosage based on the blood glucose analysis^{12,13}. Although treatment strategies based on the health monitoring via wearable and implantable devices have unique advantages, key challenges still remain.

Transdermal drug delivery patches exhibit slow drug delivery rate¹⁴, limited drug choice¹⁵, and insufficient therapeutic efficacy due to the skin barrier. Therefore, it is inappropriate for situations in which the urgent point-of-care treatment is required. On the other hand, implantable devices show rapid, localized, and high therapeutic efficacy. However, they need surgery accompanying large incision for their implantation. Moreover, conventional

implantable devices show significant mechanical mismatch with tissues mostly due to bulky and rigid power supply modules and control electronics. Such mechanical mismatches induce discomfort to the user and side effects such as collection of scar cells near the implantation site¹⁶. Although there have been novel approaches in implantable devices that recruit wireless power transmission for miniaturization and that utilize stretchable device components for softness, most cases have been applied only to electrical stimulations and/or optogenetics applications, rather than drug delivery devices aiming for rapid pharmaceutical treatment¹⁷⁻²¹.

In medical emergencies, the elapsed time after the occurrence of the symptom is a key factor that determines prognosis and survival of the patients²². Therefore, the prompt pharmaceutical treatment is very important, and a mechanically soft and minimally invasive drug delivery system that combines the advantages of wearable and implantable devices can play a critical role. Status epilepticus (SE), for example, is a fatal medical condition in which single epileptic seizure lasts longer than five min²³. When SE occurs, drugs such as diazepam should be injected immediately in order to stop the seizure²⁴. Without such prompt pharmaceutical treatment, SE often leads the patient to death. However, it is difficult for the patients under acute illness to be immediately found by caregivers. Although discovered, it takes time to transfer the patient to the hospital via ambulances for full-fledged medical treatment.

Ideally, a deformable and miniaturized device that can rapidly provide appropriate pharmaceutical treatment is implanted to subcutaneous regions of

the patient who has high-risk factors of medical emergencies such as SE. The patient also put on wearable devices wirelessly interconnected to the implanted device. See Fig. 2.1 for this health monitoring and treatment scenario. During the normal life, wearable devices monitor the key biosignals of the patient without disturbing everyday activities. If a medical emergency such as SE is detected, wearable sensor sends command signals to the wearable power transmitter for wireless power supply to the implanted drug delivery device. The rapid subcutaneous drug release stops the seizure. At the same time, an alarm signal is sent to the nearest caregivers through wireless network, so that the patient receives further medical treatment. We herein present such a device for the rapid, closed-loop, and point-of-care pharmaceutical treatment of urgent medical situations.



Figure 2.1. Monitoring and treatment scenario of the epileptic medical emergency by using SMDDI. Schematic illustrations of the scenario in which SMDDI is implanted and wearable devices are put onto a patient for continuous health monitoring and point-of-care treatment. The loaded drug is subcutaneously released in epileptic medical emergencies such as status epilepticus.

2.2 Experimental section

2.2.1 Fabrication of SMDDI Receiver Antenna

The microfabrication process starts with polyimide (PI, Poly(pyromellitic dianhydride-co-4,4'-oxydianiline), amic acid solution, Merck KGaA, Germany) coating (4000rpm, spin coating) on silicon oxide wafer (300 nm thermal silicon oxide on silicon wafer). Then, 1st Cu layer is deposited for the receiver antenna coil (4 μ m, via thermal evaporator) and patterned by a photolithographic process. Epoxy layer (SU-8 10, MicroChem Corp., USA) is coated (4000rpm, spin coating) and patterned for via hole layer. 2nd Cu layer is deposited (4 μ m, via thermal evaporator) and patterned by a photolithographic process for chip pad. Epoxy layer (SU-8 10, MicroChem Corp., USA) is coated (4000rpm, spin coating) and patterned by photolithographic process for encapsulation and contact pad opening layer.

2.2.2 Fabrication of SMDDI lid

The microfabrication process starts with 1st PI (Poly(pyromellitic dianhydride-co-4,4'-oxydianiline), amic acid solution, Merck KGaA, Germany) coating (4000rpm, spin coating) on silicon oxide wafer (300 nm thermal silicon oxide on silicon wafer). Then, 1st Al layer is deposited for etch mask of SMDDI (50nm, via thermal evaporator) and patterned by a photolithographic process. 2nd PI layer is coated and 2nd Al layer is deposited by using the same process of 1st layers. 2nd Al layer is patterned by a photolithographic process for etch mask of fuse area. Epoxy layer (SU-8 2000.5, MicroChem Corp., USA) is coated

(3000 rpm, spin coating) and patterned for bottom encapsulation layer. Pt bubble pads are deposited (30nm, via sputter) and patterned by lift-off process. 1st Cr/Au layer is deposited (10 nm/20 nm respectively, via thermal evaporator) and patterned (wet-etching process) to build fuse. Then, 2nd Cr/Au layer is deposited (30 nm/100nm respectively, via thermal evaporator) and patterned for electrical interconnect of SMDDI. Finally, epoxy layer (SU-8 10, MicroChem Corp., USA) is coated (3000 rpm, spin coating) and patterned for top encapsulation layer.

2.2.3 Fabrication of drug reservoir

The drug reservoir was fabricated by two-step molding process. First, master mold was fabricated with acrylic plate via milling process. The surface of the master mold was rinsed with ethanol and treated with oxygen plasma (O₂ 100 sccm, 0.1 mTorr, 30 W, 30 s). Then the mold was placed in an airtight container with a small dish filled with 100 μL of trichloro(1H,1H,2H,2H-perfluorooctyl)silane (FOTS, Merck KGaA, Germany) mixed to 10 mL of n-Heptane, for at least 1 hr for gas phase deposition of FOTS.

In order to make a negative of the master mold, silicon rubber (Ecoflex™ 00-30, Smooth-on, USA) part A and B was mixed in 1:1 weight ratio and poured to the surface treated master mold. After degassing the pre-polymer mixture in a desiccator, it was thermally cured at 70 °C oven over 1 hr. Fully cured silicon rubber negative was removed from the master mold and underwent gas phase deposition of FOTS as it was previously described. Then

silicon rubber 00-30 pre-polymer mixture was applied to the negative mold, and degassed in a desiccator. After thermal curing at 70 °C hot plate over 1 hr, fully cured reservoir was removed from the negative mold. Then the reservoir was encapsulated with parylene-C.

2.2.4 Integration of SMDDI to reservoir and drug loading

Before transfer process of SMDDI lid, poly(methyl methacrylate) (PMMA A11, MicroChem Corp., USA) is spin-coated on SMDDI lid for buffer layer. Polydimethylsiloxane stamp (SYLGARD™ 184, Dow Corning Corp., USA) is attached to SMDDI lid to pick up the device from wafer. Then, PI layers are patterned using dry etching process with Al etch masks (O₂ 100 sccm, 0.3 mTorr, 200 W, 20 min). Al etch masks are removed by wet etchant and the device is clearly rinsed by deionized water. The surfaces of drug reservoir and SMDDI lid are gently modified by oxygen plasma (O₂ 100 sccm, 0.1 mTorr, 100 W, 10 s) for improving affinity to adhesive (NOA 73, Norland Products Inc., USA). The device is attached on the backside of the reservoir using the adhesive. Finally, the PDMS stamp and PMMA layer are removed by using acetone.

Drug loading process is simply conducted through inlet and outlet hole of SMDDI lid. Drug is injected through inlet hole of the device using syringe with ultrathin needle. Then, the inlet hole is encapsulated with UV-responsive epoxy layer (NOA 73, Norland Products Inc., USA).

2.3 Results and discussion

2.3.1 Wireless integration of SMDDI and wearables

The system consists of a soft miniaturized drug-delivery implant (SMDDI) wirelessly integrated with a wearable electrophysiology sensor and a wearable power transmitter (Fig. 2.2a). The electrophysiology sensor is attached on the subject's head, while the SMDDI is implanted in the subcutaneous region nearby the wrist and the watch-type power transmitter is worn above the SMDDI. The location of the SMDDI and the power transmitter can be moved from the wrist to the upper arm or chest region depending on the situation (Fig. 2.3a), and other types of wearable power transmitters such as the armband or patch-type device can be used instead of the watch-type device (Fig. 2.3b,c).

Figure 2.2b shows the flowchart of the system algorithm. First, the patient should put on the wearable sensor and power transmitter on head and wrist, respectively. Because the SMDDI is placed under the skin, it may be tricky for the patient to wear the transmitter at the appropriate position for the wireless coupling between two devices. Therefore, the position alignment of the power transmitter can be assisted by the LED-based alignment indicator. Then, the sensor continuously monitors electroencephalography (EEG) signals. When seizure is detected, the system measures the elapsed time from the seizure onset. If the seizure halts within 5 min, the system returns to its monitoring state. However, if the seizure continues for more than 5 min, the system judge emergency and wirelessly sends a command signal to the power transmitter,

which generates the RF signal for wireless power transmission to SMDDI. The SMDDI receives the RF power and immediately releases the drug.

Figure 2.2c-d shows the block diagram of the entire system. The wearable electrophysiology sensor unit is an 8-channel sensing device with Bluetooth communication designed to be worn around the head (Fig. 2.4e). The collected EEG signals are conditioned by passive filters and converted to digital signals by analog-to-digital converter (ADC; ADS1299IPAGR, Texas Instruments Inc., USA). The microcontroller unit (MCU; PIC32MX250F128B-I/SS, Microchip Technology Inc., USA) processes the acquired data and transmits the result to external devices via Bluetooth module (RFduino 22301, RFDigital Corp., USA). See Figs. 2.4 and 2.5 for further details. The wearable power transmitter receives the command signal via Bluetooth module (RN42-I, Microchip Technology Inc., USA), which controls the voltage controlled oscillator (VCO; CVCO55CL-0038-0042, Crystek Corporation®, USA), RF amplifier (BGA3023, NXP Semiconductors N. V., Netherlands), and RF switch (PE42724A-Z, pSemi, USA) (Fig. 2.5g,h). If needed, the output power is attenuated by the attenuator. The RF signal is transmitted by the antenna. The SMDDI receives the RF signal and processes to DC output with the matching circuit and rectifier. The two LED indicators show the status of power transfer. If the DC output is larger than the threshold, SMDDI releases drugs for rapid pharmaceutical treatment.

The key device of the system is SMDDI (Fig. 2.2f,g; front, back). It has a dimension of $5 \times 25 \times 2$ mm (width \times length \times height), and $\sim 50\%$ of the

device volume corresponds to cavities for drug loading. The SMDDI is made of silicone rubber (Ecoflex™, Smooth-on, USA) to achieve the deformable form factor (Fig. 2.2h). The SMDDI is implanted into the subcutaneous region with minimal surgical incision, which is less than 1 cm (Fig 2.2i). Therefore, the rapid pharmaceutical treatment bypassing the skin barrier can be achieved, while burden to the patients caused by large surgical incision can be avoided (Fig. 2.2i). The wireless integration of SMDDI with wearable devices (Fig. 2.2j,k for electrophysiology sensor and watch-type power transmitter, respectively) has enabled removal of bulky and rigid components such as sensors, batteries, and data processing circuits from SMDDI. The SMDDI only has wireless power receiving units and drug delivery system, which allows its soft and miniaturized design. Such an on-demand, point-of-care, and fast pharmaceutical treatment method is particularly useful in emergency medical situations.

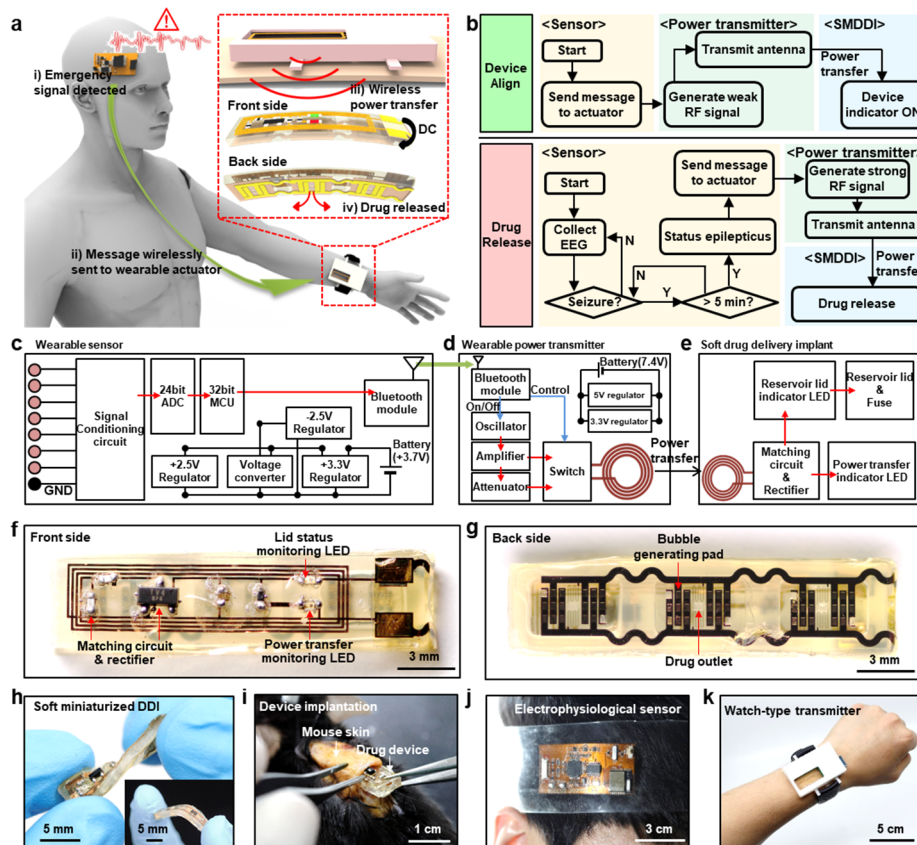


Figure 2.2. Wireless integration of SMDDI and wearable. (a) Schematic illustration of the wirelessly integrated SMDDI and wearables. Inset shows the wireless power transfer through the skin. (b) Flow chart for the wireless device coupling and drug release process. (c) Block diagram of the wearable EEG sensor showing the construction of its main circuit components. (d) Block diagram of the wearable power transmitter showing the construction of its main circuit components. (e) Block diagram of SMDDI showing the construction of its main circuit components. (f) Optical image of the front side of SMDDI. (g) Optical image of the back side of SMDDI. (h) Optical image presenting softness of SMDDI. (i) Optical image presenting implantation of SMDDI. (j) Optical image of wearable sensor. (k) Optical image wearable transmitter.

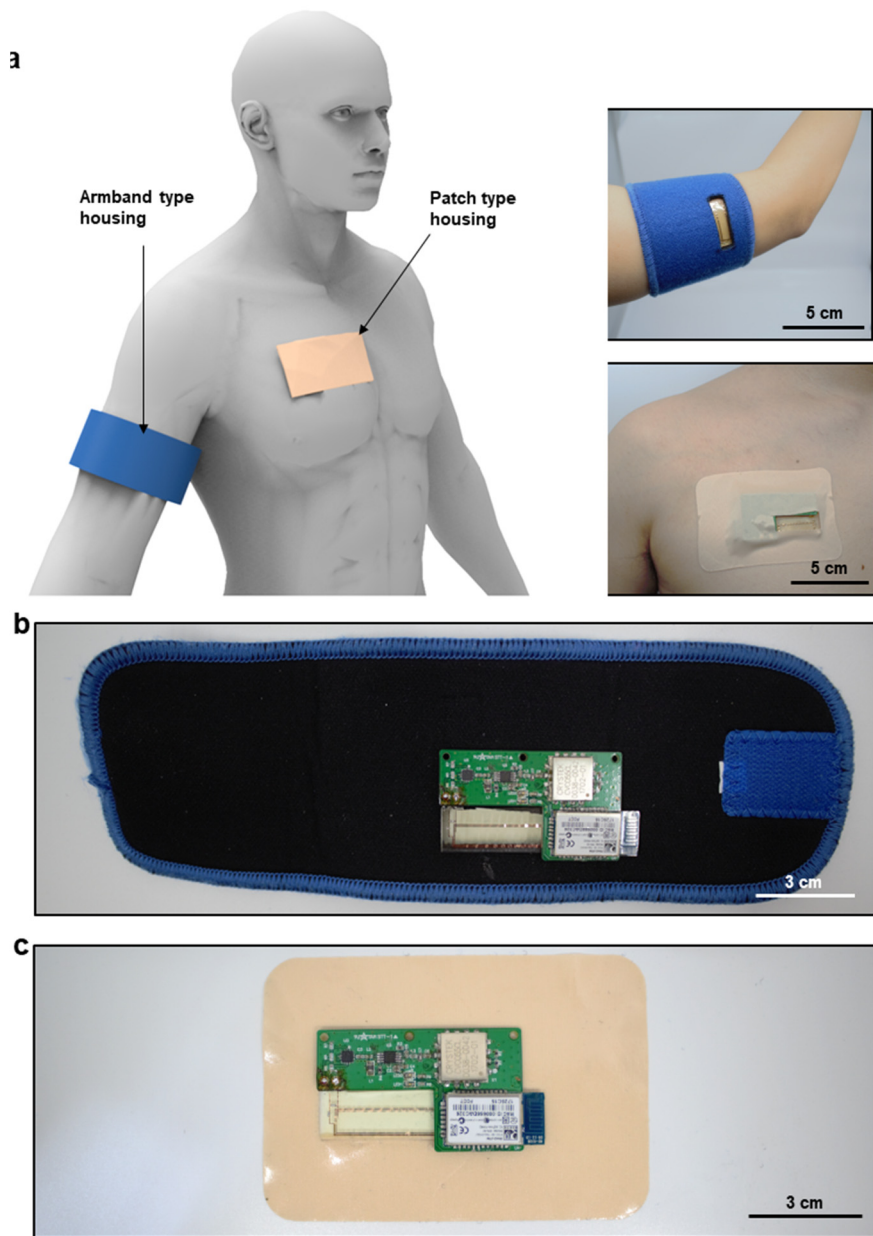


Figure 2.3. Various types of wearable power transmitters depending on the location of SMDDI. (a) Schematic illustration and images of various types of wearable power transmitters such as an armband or a patch-type device. **(b)** Inside image of the armband-type power transmitter. **(c)** Inside image of the patch-type power transmitter.

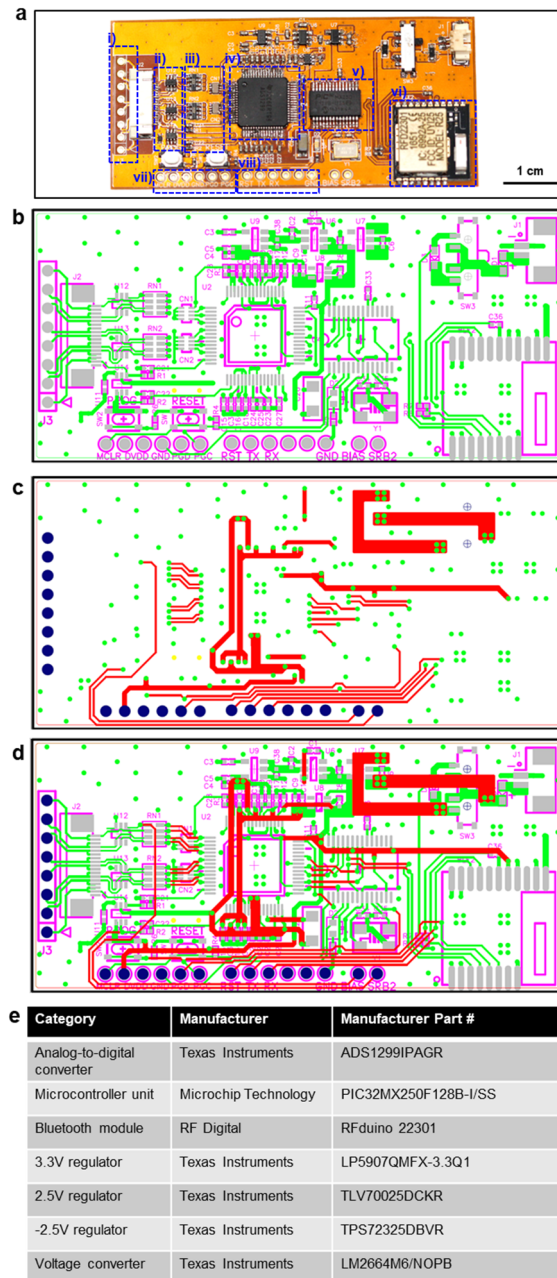


Figure 2.4. Circuit design and information of microchips for the wearable sensor. (a) Image of the wearable EEG sensor. **(b-d)**, Circuit layout on the flexible PCB for the wearable EEG sensor. **(e)** List of the chipsets used for the circuit construction.

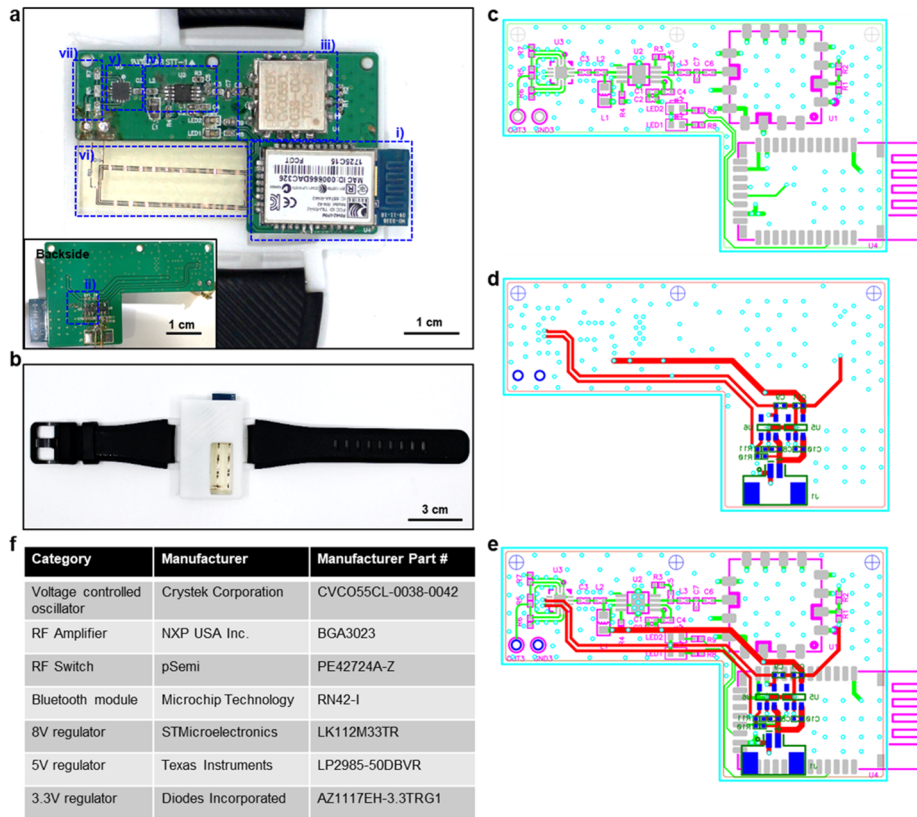


Figure 2.5. Circuit design and information of microchips for the wearable power transmitter. (a) Image of the watch-type wearable power transmitter. **(b)** Image of the wearable power transmitter assembled in the housing. **(c-e)** Circuit layout on the PCB for the wearable power transmitter. **(f)** List of the chipsets used for the circuit construction.

2.3.2 Wireless integration of the wearable and implantable device components

Figure 2.6a illustrates wireless power transmission between the wearable power transmitter and the antenna of SMDDI (front side of SMDDI) through the skin barrier. The transmitted RF signal is received by the flexible antenna of SMDDI, and converted into DC voltage through the impedance matching circuit and rectifier. The two LED indicators on the device display the condition of the device and drug release to the user. The red LED automatically turns on as power is supplied to the device and is used as an alignment key.

Figure 2.6b shows the interior of the watch-type power transmitter. The printed circuit board (PCB) was designed as a double-sided board for the small form factor. The Bluetooth module receives the signal sent from the sensor and controls the VCO, RF amplifier, and switch to generate an appropriate RF signal. The generated RF signal is transmitted to the transmit antenna and wirelessly provides power to SMDDI. Because LED indicators of SMDDI should be observed from the outside, the transmit antenna was fabricated separately on a transparent PDMS substrate for the see-through design.

To release drug from the reservoir, a high voltage over the threshold should be applied to the lid. The receiver coil size is 20 mm×4 mm to fully exploit the implant size. The wireless voltage induction system should induce maximum voltage across the receiver coil with a given power dissipated in a lossy human tissue. This is an optimization problem over the space of current

sheets \mathbf{J}_s placed above the skin. Since the induced voltage at the receiver coil is proportional to the change rate of magnetic flux going through the coil area S , it is equivalent to find the current distribution that maximizes the *voltage gain* defined as follows.

$$\eta = \frac{|\int_S \omega \mathbf{H} \cdot d\mathbf{S}|^2}{\int_{tissue} \omega \epsilon'' |\mathbf{E}|^2 dr^2}$$

where ω is the radian frequency of induced magnetic field and ϵ'' is the imaginary part of dielectric permittivity of tissue. The denominator of the voltage gain incorporates the power loss inside tissue due to oscillating electric fields.

When the tissue is modeled as a multilayered medium composed of different dielectric properties, the above optimization problem can be solved analytically (See supplemental). The simulation of the coupling between two physical coils shows that a highest voltage gain is obtained at ~ 40 MHz (Fig. 2.6c). The matching network at the transmit coil is included to suppress the power reflection at 40 MHz, resulting the minimum return loss (S11) measured with vector network analyzer (Fig. 2.6d). The transmitter generates RF power in two different levels, one for initial checking of device alignment and the other for drug release. When the RF signal below 10 dBm is transmitted, SMDDI receives voltage less than 2 V, which does not trigger the drug release but can be used for LEDs indicating the system condition. When emergency biosignals are detected, however, the RF signal as high as 19 dBm is supplied to generate the high voltage (10 V) and to deliver the drug immediately (Fig.

2.6e). Figure 2.6f shows the magnetic field created by the transmitter, which confirms the magnetic field energy is mainly confined in subcutaneous region to operate the implanted SMDDI. The field strength attenuates fast beyond the location of SMDDI because the waves are mostly evanescent.

Two LEDs (red and green) in SMDDI indicate the device condition (Fig. 2.6g,h; schematic illustrations, corresponding images). First, the LEDs are used as an alignment key between the transmitting and receiving RF antenna. The LEDs become brighter as the alignment with the external antenna improves. Therefore, the wearable power transmitter and the implanted SMDDI can be aligned upon the maximum brightness of the LEDs. The green LED indicates the drug delivery condition by displaying the lid status. If the lids remain intact without breakage, the circuit including the lid and the green LED forms a closed loop to turn the green LED on. In the drug release mode, the lid is ruptured and the loop is disconnected, which turns the green LED off, while the red LED is still on to confirm a good alignment.

Figure 2.6i,j show the stability of wireless power transfer to SMDDI which is under displacement or mechanical deformation. Voltage gain simulated over the multilayer tissue model under the device displacement along x-axis is not decreased up to the displacement of 4 mm, and that along y-axis still remains above 80 % up to the displacement of 2 mm (Fig. 2.6i). Therefore, the small displacement of the transmitter or SMDDI does not critically affect the wireless power transmission performance. Armband or patch-type devices can be used for better fixation and alignment (Fig. 2.4) Moreover, bending of

the antenna does not reduce the voltage gain of the device unless the bending radius of the antenna is as small as 50 mm (Fig. 2.6j). Therefore, bending of SMDDI under the skin, which can be up to 100 mm of the bending radius, does not affect the power transmission. Figure 2.6k demonstrates how the variation of tissue compositions affects the performance of wireless power transfer to SMDDI. When the fat thickness varies in the multilayered model, the change in voltage gain is insignificant. Figure 2.6l shows the output voltage variation under various conditions which was studied through 2.6i-k. The colored area of the graph shows that there is a significant difference in the output voltage between 19 dBm and 10 dBm of the input RF power. Because there is a wide safe-zone between two input powers, unwanted drug release is unlikely to occur during device alignment process.

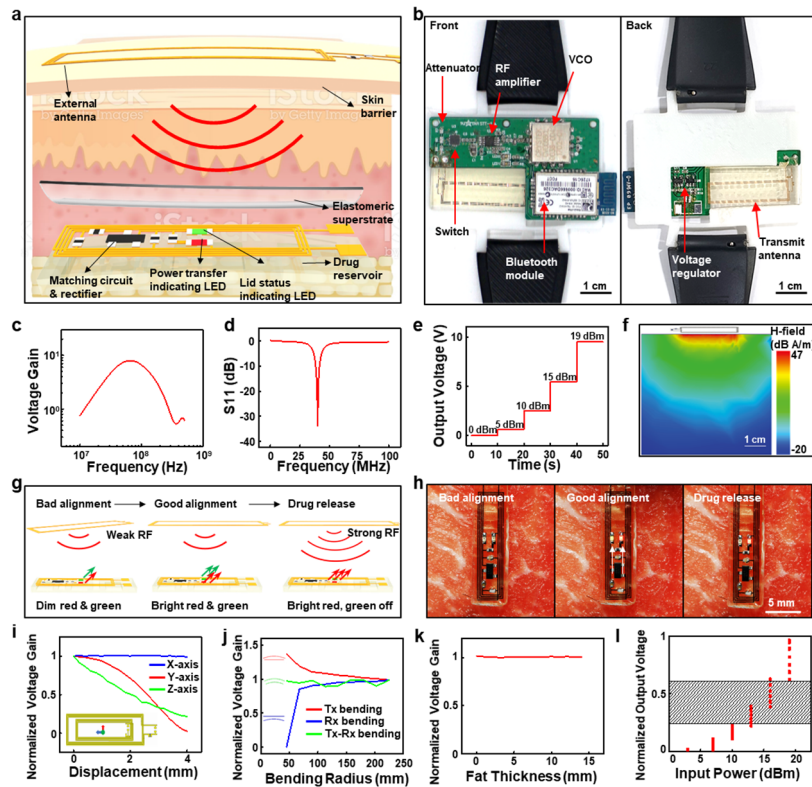


Figure 2.6. Wireless coupling by voltage induction to SMDDI. (a) Simulation result of the efficiency versus frequency. (b) Camera images of wireless power transmitter integrated in watch-type device. (c) Voltage gain measurement depending on RF signal frequency. (d) S11 measurement of the transmitter coil. (e) Output voltage measured under different RF signal strengths with the lid resistance of 5 k Ω . (f) Simulated result of electromagnetic field distribution. (g) Schematic illustrations for brightness changes of LED indicators during device coupling and drug release. (h) Images for brightness changes of LED indicators during device coupling and drug release. (i) Simulation of efficiency changes under displacements in x, y, and z axis. (j) Output voltage measurement under displacements x, y, and z axis. (k) Simulation of efficiency changes by tissue component variation. (l) Simulation of normalized output voltage affected by displacements ($|\Delta y| \leq 1.5$ mm, $|\Delta z| \leq 1$ mm) and tissue composition changes (2 mm \leq fat thickness ≤ 10 mm) under various input powers.

2.3.3 Fabrication and drug delivery mechanism of SDMMI

Figure 2.7a shows an exploded view of the drug reservoirs and its lid that are located at the backside of SMDDI. In order to minimize the size of SMDDI, the both sides are used. The front side of the device contains an antenna, while the encapsulation lids to be ruptured during the drug release process is located at the backside. The drug reservoirs fabricated with the silicone-based elastomer (Ecoflex™, Smooth-On, Inc., USA; modulus: 68.9 kPa) to be mechanically comparable to tissues. Because silicone elastomer itself cannot block the drug leakage and water penetration between the reservoir and surrounding tissues, multiple thin film encapsulation layers of parylene (~ 1 μm) and SU8 (Bottom layer: ~ 500 nm, Top layer: ~ 10 μm), which are well-known water blocking layers, are utilized. The Au interconnects and Pt pads (Fig. 2.7a) are used as electrodes for water decomposition via electrolysis. The Pt pads contact with the aqueous drug solution loaded inside the reservoir (Fig. 2.7b). High voltage between anode and cathode generated by the wireless power transmission rapidly electrolyzes water in the solution into oxygen and hydrogen vapor, which rupture the lid and push the drug via the outlet (Fig. 2.7c). When the outlet part of the lid is ruptured during the drug release process, it disconnects the fuse and increases the overall resistance of the lid. Therefore, the green LED indicator of the front side of the device turns off.

Figure 2.7d shows the drug inlet and outlet of the reservoir. The drug is injected into the reservoir through the inlet via an ultrathin syringe needle followed by an encapsulation of the inlet. Detailed device fabrication procedure

are described in Experimental section and Fig. 2.8. Time-lapse images of the drug release (Fig. 2.7e) show that gas bubbles are vigorously generated as soon as the wireless power transfer is applied to SMDDI (within 0.6 s). As the internal pressure reaches critical point, the outlet including the fuse is destroyed (~ 1 s), and the drug is ejected from the reservoir due to high internal pressure induced by generated bubbles (~ 10 s). The intact and ruptured lid before and after the drug release is shown in Fig. 3f. After the rupture, the resistance of the closed-circuit in SMDDI increases $\sim 1,000$ times (Fig. 2.7g), which turns off the green LED as indication of the drug release. The red LED is still turned on, which shows the good alignment between transmitting and receiving antennas.

Pt layers are added on the Au layer for the bubbling pads. The water decomposition reaction is accelerated via catalysis, which reduces the time required for drug release. Without the Pt layer, drug release rate is ~ 3 times slower than that with the Pt layer (Fig. 2.7h). Because SMDDI has to release the drugs only in emergencies, two types of operation modes are used. When low power (2 V) is applied to SMDDI, no drug release occurs. When high power (6 V) is applied, $\sim 70\%$ of the drugs are released within 30 s (Fig. 2.7i).

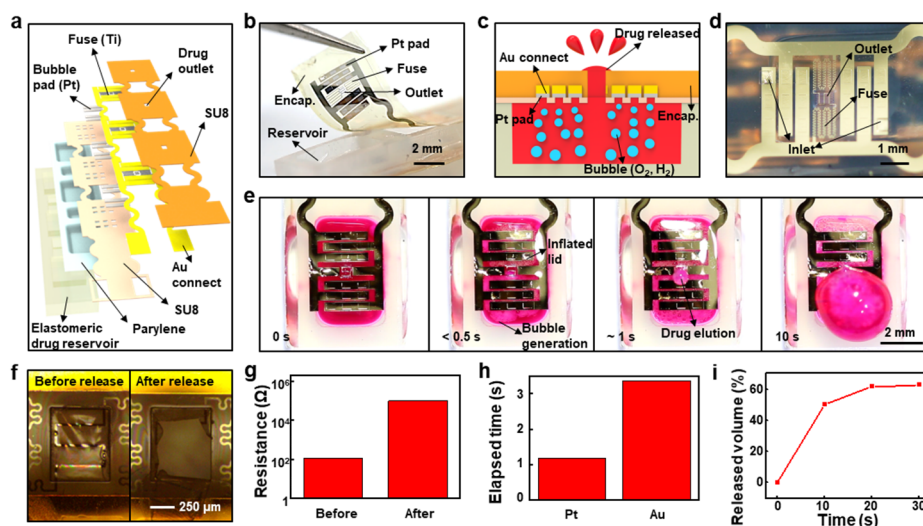


Figure 2.7. Drug release from SMDDI. (a) Exploded view of the back side of SMDDI. (b) Optical image of the lid and reservoir of SMDDI. (c) Schematic illustration of drug release mechanism. (d) Magnified optical image of the drug inlet and outlet of SMDDI. (e) Time-lapse optical images of the drug release process. (f) Optical images of the fuse before (left) and after (right) drug release. (g) Resistance change after lid opening. (h) Enhanced efficiency of drug release. (i) Drug release profile of SMDDI *in vitro*.

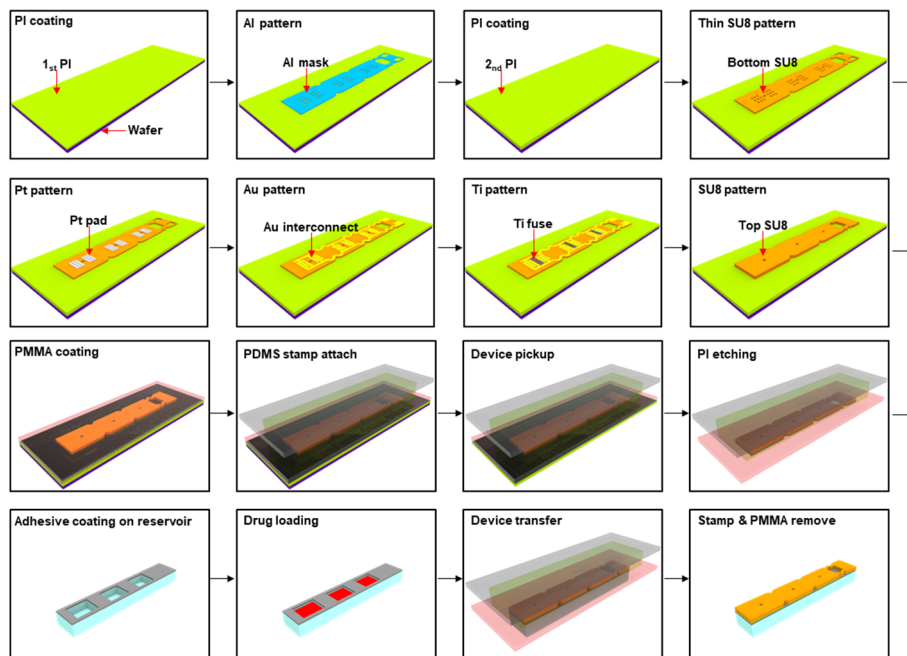


Figure 2.8. Fabrication process of the backside of SMDDI. Step-by-step illustration of fabrication procedures for the backside of SMDDI such as the lid fabrication and drug injection.

2.3 Conclusion

In summary, we have developed a wirelessly-integrated system for SE treatment, which consists of SMDDI, wearable sensor, and power transmitter. The system takes advantages of wearable and implantable devices by utilizing wireless control and power transmission technology. The wearable devices monitor EEG and wirelessly send RF power to SMDDI through near-field coil pairs for on-demand drug-release. This wireless integration enables mechanical softness and miniaturized design of SMDDI by removing bulky and rigid components such as batteries and control units from drug delivery implant. Further large-scale animal experiments and human tests are required in the future for system optimization and clinical translation. This advanced implantable drug delivery system is a step forward to the next-generation soft bioelectronics.

References

1. Son, D. *et al.* Multifunctional wearable devices for diagnosis and therapy of movement disorders. *Nat. Nanotechnol.* **9**, 397–404 (2014).
2. Schwartz, G. *et al.* Flexible polymer transistors with high pressure sensitivity for application in electronic skin and health monitoring. *Nat. Commun.* **4**, 1858–1859 (2013).
3. Gao, W., Ota, H., Kiriya, D., Takei, K. & Javey, A. Flexible Electronics toward Wearable Sensing. *Acc. Chem. Res.* **52**, 523–533 (2019).
4. Choi, S. *et al.* Highly conductive, stretchable and biocompatible Ag–Au core–sheath nanowire composite for wearable and implantable bioelectronics. *Nat. Nanotechnol.* **13**, 1048–1056 (2018).
5. Cho, H. R. *et al.* Wearable/disposable sweat-based glucose monitoring device with multistage transdermal drug delivery module. *Sci. Adv.* **3**, e1601314 (2017).
6. Gao, W. *et al.* Fully integrated wearable sensor arrays for multiplexed in situ perspiration analysis. *Nature* **529**, 509–514 (2016).
7. Lee, H. *et al.* A graphene-based electrochemical device with thermoresponsive microneedles for diabetes monitoring and therapy. *Nat. Nanotechnol.* **11**, 566–572 (2016).
8. Hong, Y. J. *et al.* Multifunctional Wearable System that Integrates Sweat-Based Sensing and Vital-Sign Monitoring to Estimate Pre-/Post-Exercise Glucose Levels. *Adv. Funct. Mater.* **28**, 1–12 (2018).
9. Kaszala, K. & Ellenbogen, K. A. Device sensing: Sensors and algorithms for pacemakers and implantable cardioverter defibrillators.

- Circulation* **122**, 1328–1340 (2010).
10. Proietti, R. *et al.* Closed loop stimulation is effective in improving heart rate and blood pressure response to mental stress: Report of a single-chamber pacemaker study in patients with chronotropic incompetent atrial fibrillation. *PACE - Pacing Clin. Electrophysiol.* **35**, 990–998 (2012).
 11. Russo, V. *et al.* The effect of dual-chamber closed-loop stimulation on syncope recurrence in healthy patients with tilt-induced vasovagal cardioinhibitory syncope: A prospective, randomised, single-blind, crossover study. *Heart* **99**, 1609–1613 (2013).
 12. Cobelli, C., Renard, E. & Kovatchev, B. Artificial Pancreas: Past, Present, Future. *Diabetes* **60**, 2672–2682 (2011).
 13. Doyle, F. J., Huyett, L. M., Lee, J. B., Zisser, H. C. & Dassau, E. Closed-loop artificial pancreas systems: Engineering the algorithms. *Diabetes Care* **37**, 1191–1197 (2014).
 14. Pegoraro, C., MacNeil, S. & Battaglia, G. Transdermal drug delivery: From micro to nano. *Nanoscale* **4**, 1881–1894 (2012).
 15. Banga, A. K., Donnelly, R. & Stinchcomb, A. L. Transdermal drug delivery. *Ther. Deliv.* **4**, 1235–1238 (2013).
 16. Kumar, A. & Pillai, J. *Implantable drug delivery systems: An overview. Nanostructures for the Engineering of Cells, Tissues and Organs: From Design to Applications* (2018). doi:10.1016/B978-0-12-813665-2.00013-2
 17. Park, S. Il *et al.* Soft, stretchable, fully implantable miniaturized

- optoelectronic systems for wireless optogenetics. *Nat. Biotechnol.* **33**, 1280–1286 (2015).
18. Shin, G. *et al.* Flexible Near-Field Wireless Optoelectronics as Subdermal Implants for Broad Applications in Optogenetics. *Neuron* **93**, 509-521.e3 (2017).
 19. Koo, J. *et al.* Wireless bioresorbable electronic system enables sustained nonpharmacological neuroregenerative therapy. *Nat. Med.* **24**, 1830–1836 (2018).
 20. Agrawal, D. R. *et al.* Conformal phased surfaces for wireless powering of bioelectronic microdevices. *Nat. Biomed. Eng.* **1**, 0043 (2017).
 21. Ho, J. S. *et al.* Wireless power transfer to deep-tissue microimplants. *Proc. Natl. Acad. Sci.* **111**, 7974–7979 (2014).
 22. Blackwell, T. H. & Kaufman, J. S. Response Time Effectiveness: Comparison of Response Time and Survival in an Urban Emergency Medical Services System. *Acad. Emerg. Med.* **9**, 288–295 (2002).
 23. Brophy, G. M. *et al.* Guidelines for the Evaluation and Management of Status Epilepticus. *Neurocrit. Care* **17**, 3–23 (2012).
 24. Alldredge, B. K. *et al.* A comparison of lorazepam, diazepam, and placebo for the treatment of out-of-hospital status epilepticus. *N. Engl. J. Med.* **345**, 631–7 (2001).

***Some contents of this chapter will be published in a scientific journal.**

Chapter 3. Instrumented Surgical Endoscopes with Integrated Graphene-Hybrid Electronics and Theranostic Nanoparticles

3.1 Introduction

Conventional endoscopes contain a flexible tube fitted with a camera and a light fixture near the tip for some maneuverability and simultaneous visualization of gastrointestinal tract. More advanced endoscopes allow for greater accuracy during maneuvering within tightly spaced orifices, and offer both therapeutic and diagnostic features during visual observation of cancer distribution, tissue biopsy, and resection of tumors and polyps¹. In spite of the proven utility of endoscope-based procedures, there are important limitations. For example, resections may cause inflammations with marginal insight into the form and stage of the tumor cells. Small segments of resected cancerous tissue typically do not represent the physiological dynamics of the entire cancer, suggesting that more targeted therapies and diagnostics are necessary^{1,2}. Radio frequency (RF) ablation and localized photo-/chemo- therapies could serve as viable alternatives to surgical resections^{3,4}. In both instances, intraprocedural mapping using multi-modal sensors⁵⁻⁸ and localized, controlled delivery/actuation⁹⁻¹³ are required to identify the precise location^{7,8} and physicochemical properties^{5,6} of the targeted growth and proceed necessary

treatments. A well-designed system that can sense and concurrently deliver⁹ and activate therapeutic agents¹⁰⁻¹³ in confined area near tumors, therefore, constitutes a vast improvement over existing practices in endoscope-based treatment strategies.

Here, we demonstrate a multifunctional sensing and therapeutic endoscope system to treat diseases like organ-specific cancers (Fig. 3.1 and 3.2 for schematic illustrations and corresponding images). This ‘smart’ endoscope platform contains transparent graphene-hybrid electronics, which provides impedance-/pH- based monitoring and RF ablation therapy to characterize and remove cancer cells. Additional sensors for monitoring mechanical contact, and temperature provide accurate physiological sensing during cancer detection and ablation. In addition to graphene-hybrid electronics, the system contains custom-designed theranostic nanoparticles (NPs) that can target/treat tumors by delivering photo- and chemo-therapeutic agents, activated by external stimuli in confined regions.

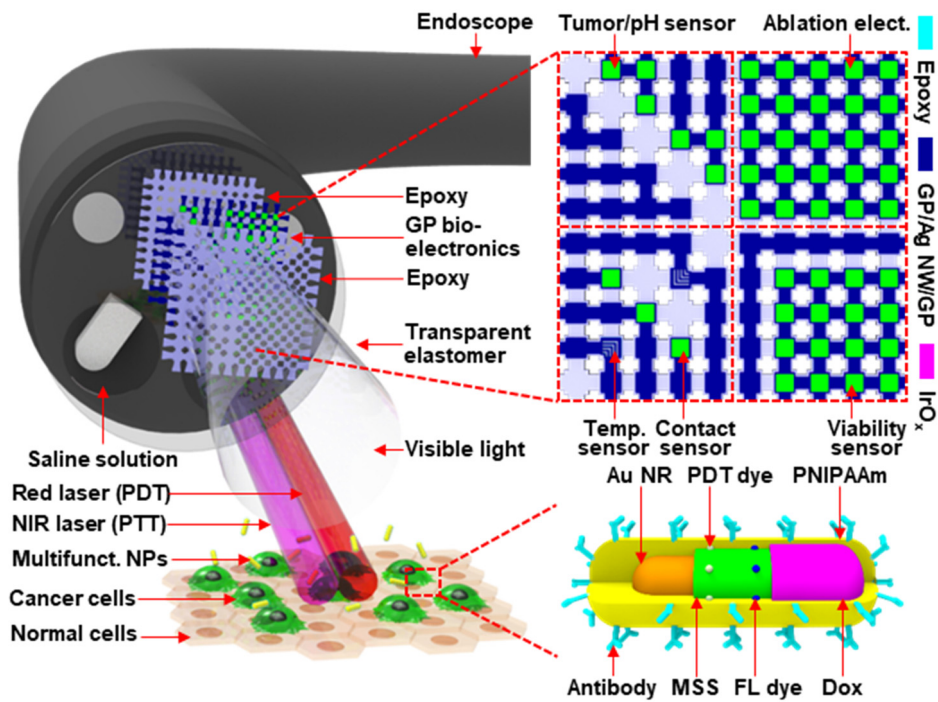


Figure 3.1. Schematic illustrations of a multifunctional endoscope system. Schematic illustrations of the design strategy and mode of use for the multifunctional endoscope system based on transparent graphene bio-electronic devices and theranostic nanoparticles.^{30,31}

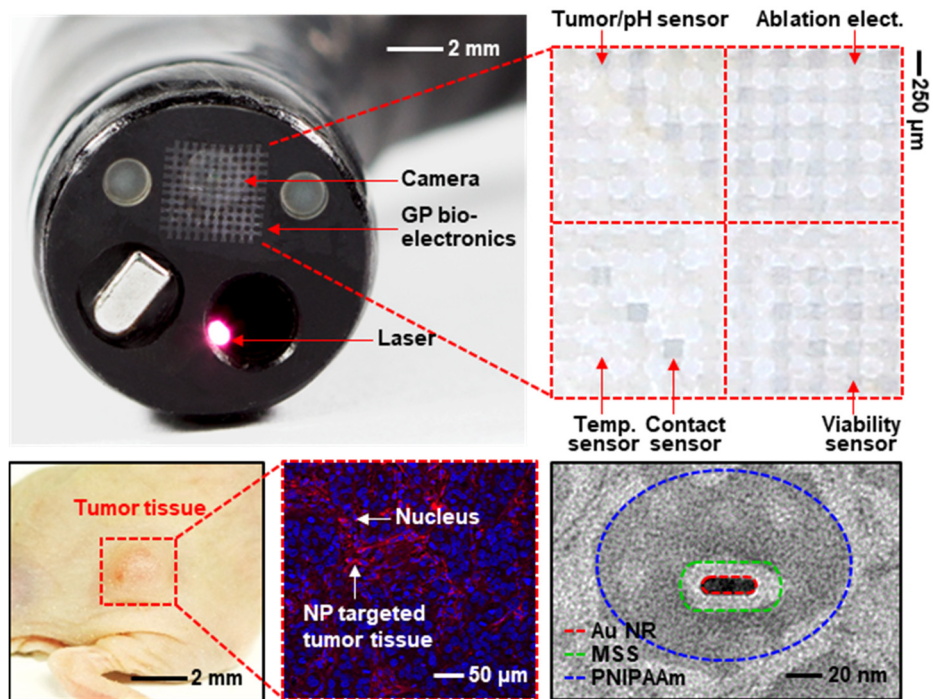


Figure 3.2. Representative images of a multifunctional endoscope system. Bottom frames show an optical camera image of NP-targeted HT-29 tumor grown in the mouse sub-dermis (left), a confocal microscope image of HT-29 tissues after NP-targeting (middle), and a TEM image of a designed theranostic NP (right).^{30,31}

3.2 Experimental section

3.2.1 Synthesis and transfer of graphene.

Graphene is synthesized by a chemical vapor deposition process³⁰, in which a roll of copper foil (Alfa Aesar, 46365) is first inserted into a 1-inch-wide tubular quartz reactor and heated to 1000 °C under an 8 sccm flow of H₂ at 80 mtorr. Once at temperature the sample is annealed for 30 min, after which a 20 sccm flow of CH₄ gas is added to the continuous H₂ and the sample is left for another 30 min. Finally, the sample is rapidly cooled to room temperature under H₂. The resulting graphene is spin-coated with PMMA A4 (Microchem) at 3000 rpm. A mild oxygen plasma treatment is then applied to help remove the graphene on the back side of copper foil and the copper layer is dissolved by a Ni etchant (Transene, Ni etchant type 1). Once the copper is removed, the PMMA-supported graphene is washed three times with ultrapure distilled water and transferred to the target substrate. Once the residual water is fully evaporated, the PMMA layer is removed with acetone.

3.2.2 Fabrication of graphene-hybrid devices.

The microfabrication process begins with the deposition of a sacrificial nickel layer (thermal evaporation, 100 nm) on a silicon-handle wafer with a bottom epoxy layer patterned using SU8-2 (Microchem). Next, a GP/Ag NW/GP structure is fabricated by transferring the bottom GP layer as described above and spin coating on it at 2000 rpm with an Ag NW solution (Nanopyxis, 0.5 wt% in IPA) that is then annealed at 130 °C for 1 min. Then, top GP layer

is transferred on them. To enhance the sensitivity of temperature monitoring the resistance of the Ag NW/GP layers is increased by photolithographic patterning and reactive ion etching to selectively remove Ag NWs from the active sites of the sensors. External parts require for in-vitro, ex-vivo and in-vivo experiments are also fabricated with active site. These consist of a polyimide layer formed by curing amic acid precursors (Sigma Aldrich, 431176) and a thermally evaporated Au/Cr metal layer, both of which are patterned using photolithography and dry/wet etching processes.

3.2.3 Selective electroplating of iridium oxide (IrO_x).

Prior to electroplating IrO_x, the graphene-hybrid electrodes are immersed in a 20 mM AuCl₃ (Sigma-aldrich, 334049) solution for 10 min to assist in forming an even IrO_x film. For the selective electroplating of these Au-doped graphene-hybrid composites, an IrO_x solution is prepared by dissolving 150 mg of iridium tetrachloride (Alfa Aesar, 12184) in 100 mL of ultrapure distilled water by stirring for 20 min. A 1 mL aliquot of aqueous 30% H₂O₂ (Sigma-aldrich, 214743) is then added and stirred for 10 min, after which 500 mg of oxalic acid dihydrate (Sigma-aldrich, 247537) is added and stirred for another 10 min. Finally, anhydrous potassium carbonate (Alfa Aesar, 12609) is used to adjust the solution pH to 10.5. The resulting solution is stored at room temperature for one week to stabilize iridium ions, resulting in a light-violet color. Electrodeposition is performed by the three-electrode method using an electrochemical analyzer (CHI instrument, CHI660E). Chronopotentiometry is

conducted at around 0.7 V for 5 min across the graphene-hybrid working electrode, the Pt wire counter electrode, and the Ag/AgCl reference electrode.

3.2.4 Ex-vivo tumor sensing.

The tumor sensor is based on measuring the impedance of normal and HT-29 tissues resected from a mouse model (BALB/c-nude mouse). The resected tissues are positioned on the counter and working electrode, which are then connected to an electrochemical analyzer (CHI instrument, CHI660E) for the two electrode method.

3.2.5 pH sensing.

The electrochemical growth of IrO_x films from an aqueous solution is known to result in a hydrous structure that exhibits multiple states during reduction and oxidation. Furthermore, the zeta potential of the IrO_x film surface is dependent on the pH of the solution and directly affects the open circuit potential (OCP). The pH dependence of OCP is characterized using an electrokinetic analyzer (Anton Paar, SurPASS), wherein the pH sensor is an electrochemical analyzer (CHI instrument, CHI660E) operating by two electrode method using pH sensitive graphene-hybrid working electrode and Au doped GP/AgNW/GP counter electrode. The OCP is calibrated using a pH buffer solution (Alfa Aesar), and based on this data, the measured OCP values are converted to pH to produce results comparable with a commercial pH meter (Thermo Scientific Orion, STARA2115). *In-vivo* pH sensor demonstration

measures pH value of tissues and blood of mouse directly contact to each of them. During pH measurement of blood, heparin was treated to prevent coagulation (5 IU heparin/mL of blood).

3.2.6 RF ablation and related sensing.

RF ablation is conducted using the experimental setup, in which the graphene-hybrid electronics is connected to three different analyzers. An electrochemical analyzer is used to measure the impedance of the contact sensor, the tumor detector and the viability sensor, which are all made from the same materials but have their functionality customized for each application. RF ablation is conducted by wiring the ablation electrode to an RF generator (DAIWHHA corporation, MEDITOM 150 basic, 200kHz), with the temperature being continuously monitored by measuring the change in the sensor resistance with a digital multimeter (National instruments, USB-4065), with the temperature change confirmed by a commercial IR camera (FLIR, FLIR E8). To determine the effectiveness of the process, the tissue viability is measured before and after ablation.

3.3 Results and discussion

Clinical applications of this smart endoscope system for the treatment of colon cancer begin with the intravenous injection of NPs (Fig. 3.1 and 3.2) that actively target colon cancer cells (HT-29) due to the specific antibodies (cetuximab) that are conjugated on NPs. Fluorescence dyes that are also loaded on the NPs provide optical feedback as to the spatial distribution of cancer cells, with the uptake of NPs by cancerous cells. The endoscope guides lasers through optical fibers directly to cancer suspicious sites. These are observable through the integrated transparent graphene-hybrid electronics having an overall transmittance of ~80%. The graphene-hybrid electronics provides additional analysis of the tumor distribution and detects specific tumors. Once detected and identified, large areas of cancerous tissue are resected using forceps through the endoscope and followed by RF ablation using the active graphene-hybrid electronics (Fig. 3.1 and 3.2). Feedback modulation of this ablation therapy is based on continuous monitoring of temperature, contact, and cell viability. Locally triggered photothermal (PTT)-, photodynamic (PDT)-, and chemo-therapy induced by gold nanorod (Au NR) core, PDT dye, and doxorubicin (Dox) loaded in mesoporous silica shell (MSS) irradiated with a near infrared (NIR) or red laser (Fig. 3.1 and 3.2, left) effectively destroy any residual cancer cells around the surgically treated area. The thermosensitive poly(N-isopropylacrylamide) (PNIPAAm) shell prevents the Dox from being released without NIR laser ($\lambda = 800$ nm) irradiation. After surgery, the used graphene-hybrid electronics is detached from the endoscope to be cleaned,

sterilized¹⁴ and reused. Note that the graphene-hybrid electronics can be readily bent and stretched during installation and removal thanks to the high degree of mechanical deformability from ultrathin structure^{15,16} and intrinsic material property^{17,18}.

In the current system, the electronics is constructed based on graphene-hybrid (Fig. 3.3; schematic diagram and scanning electron microscopy (SEM) images), CVD-grown graphene^{17,18} modified with Au chemical doping and iridium oxide (IrO_x) deposition¹⁹. Ag nanowires are embedded to boost conductivity²⁰. Au doping on graphene helps uniform IrO_x plating. This hybrid structure provides excellent transparency (Fig. 3.4a). By selectively electroplating the IrO_x onto active sites, a low contact impedance can be achieved that is well suited for device-tissue interfacing 3.4b. The stability of graphene-hybrid in biofluid and at various temperatures (including hot steam for sterilization) is confirmed and through multiple cyclic voltammetry tests.

Upon completion of micro-fabrication on a rigid substrate, the graphene-hybrid electronics is transfer-printed onto a pre-shaped PDMS segment to create a flexible and stretchable electronic system. The tumor sensor, ablation electrode and viability sensor are characterized, *ex-vivo*, using resected HT-29 tissues and normal tissues from BALB/c-nude mouse model. The tumor sensor is able to differentiate between normal tissues and HT-29 tissues by measuring the impedance difference (Fig. 3.5a,b). Shifts in pH levels around tumors during rapid metabolization serve as another important marker²¹. We

monitored pH by measuring changes in the open circuit potential (OCP)¹⁹, since the surface zeta potential of graphene-hybrid exhibits pH dependence (Fig. 3.5c). The *ex-vivo* RF ablation studies in the BALB/c-nude mouse are conducted on thigh tissues, whose temperature distribution and extent of the lesions are imaged by IR and optical cameras, respectively (Fig. 3.6). To provide effective control of the lesion profile, conformal contact and temperature are constantly monitored throughout the ablation procedure (Fig. 3.7). Finally, the viability sensor provides a way of differentiating between bare and ablated tissues during and after RF ablation by reporting localized changes in impedance (Fig. 3.8).

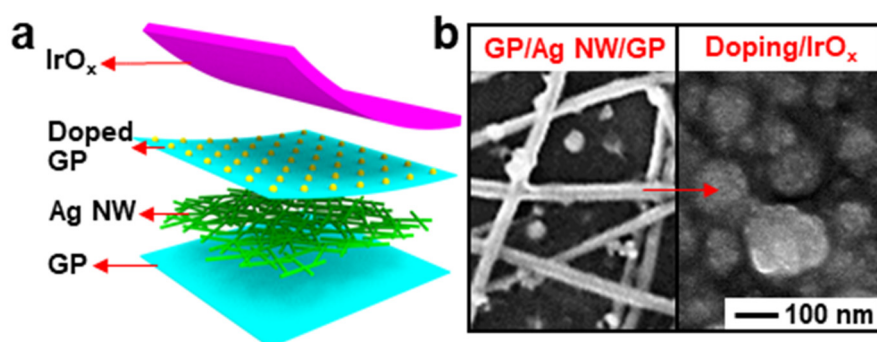


Figure 3.3. Composition of the graphene-hybrid. (a) Schematic illustration of the graphene-hybrid in the exploded view. (b) SEM images before and after the IrO_x electrodeposition (right).^{30,31}

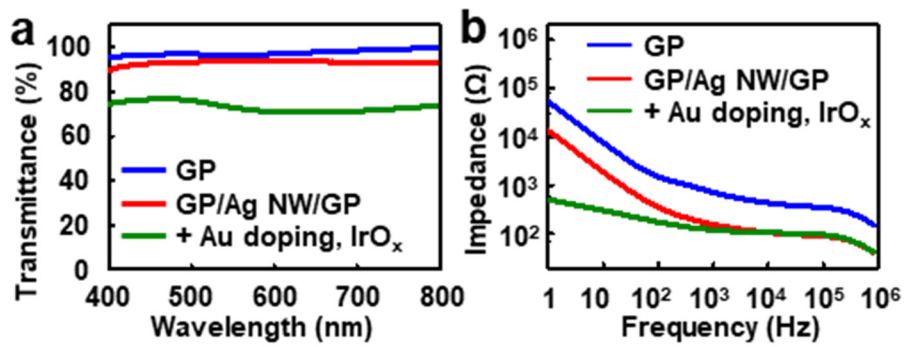


Figure 3.4. Characterizations of the graphene-hybrid. (a) Optical transmittance measurement of the graphene-hybrid. **(b)** Bode plots of the graphene-hybrid.^{30,31}

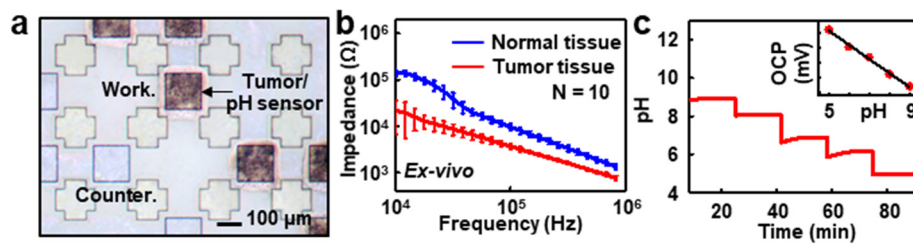


Figure 3.5. Graphene-hybrid based tumor and pH sensor. (a) Optical microscope image of tumor and pH sensor. **(b)** Impedance measurement of tumor (HT-29) and normal tissues ex-vivo (mouse number = 10). **(c)** pH monitoring in sequential additions of the acidic buffer solution). Working and counter electrodes for electrochemical measurement are shown in the top frame.^{30,31}

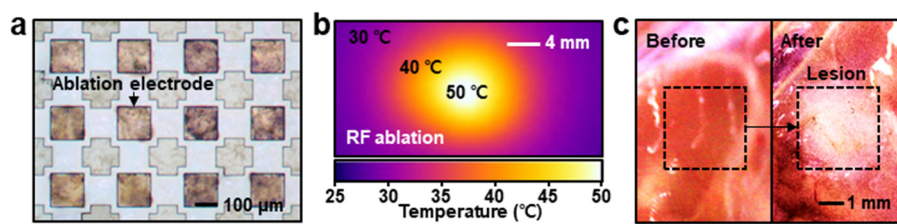


Figure 3.6. Graphene-hybrid based RF ablation electrode. (a) Optical microscope image of RF ablation electrode. **(b)** IR camera image during the RF ablation. **(c)** Optical camera images before and after RF ablations of mouse thigh tissues *ex-vivo*.^{30,31}

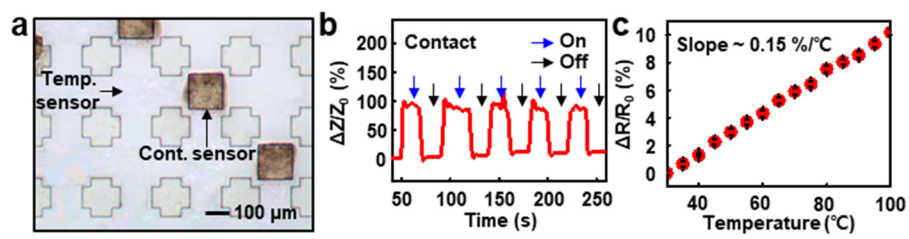


Figure 3.7. Graphene-hybrid based temperature and contact sensor. (a) Optical microscope image of temperature and contact sensor. **(b)** Impedance measurements in on- and off-contacts. **(c)** Calibration curve of the temperature sensor.^{30,31}

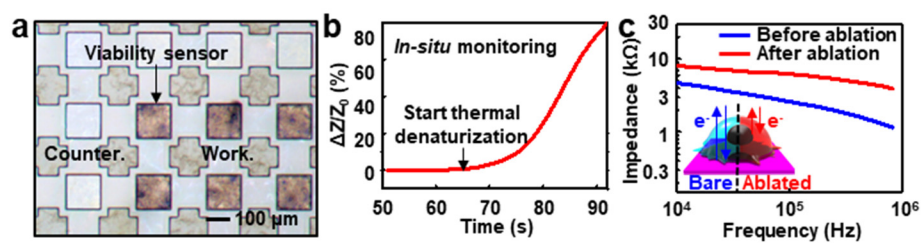


Figure 3.8. Graphene-hybrid based viability sensor. (a) Optical microscope image of viability sensor. **(b)** *In-situ* impedance measurement during the thermal denaturation of mouse tissues. **(c)** Impedance measurement before and after the RF ablation of tumor tissues).^{30,31}

3.4 Conclusion

In summary, the mechanics, materials and geometries of sensors and electronics developed for the advanced, multifunctional endoscope systems presented in this study have the potential to dramatically speed up and improve the efficacy of minimally invasive surgical procedures. These devices facilitate access via minimal incisions/resection areas, and provide a significant amount of feedback about the target diseases with concurrent therapeutic delivery. *In-vivo* animal experiments as well as *in-vitro* and *ex-vivo* validations of the current systems highlight the utility of this technology in translational medicine.

References

1. Balog, J. *et al.* Intraoperative tissue identification using rapid evaporative ionization mass spectrometry. *Sci. Transl. Med.* **5**, 194ra93 (2013).
2. Tennant, D. A., Duran, R. V. & Gottlieb E. Targeting metabolic transformation for cancer therapy. *Nat. Rev. Cancer* **10**, 267-277 (2010).
3. Vanneman, M. & Dranoff, G. Combining immunotherapy and targeted therapies in cancer treatment. *Nat. Rev. Cancer* **12**, 237-251 (2012).
4. Chu, K. F. & Dupuy, D. E. Thermal ablation of tumors: biological mechanisms and advances in therapy. *Nat. Rev. Cancer* **14**, 199-208 (2014).
5. Kim, D.-H. *et al.* Materials for multifunctional balloon catheters with capabilities in cardiac electrophysiological mapping and ablation therapy. *Nat. Mater.* **10**, 316-323 (2011).
6. Kim, D.-H. *et al.* Electronic sensor and actuator webs for large-area complex geometry cardiac mapping and therapy. *Proc. Natl. Acad. Sci.* **49**, 19910-19915 (2012).
7. Xu, L. *et al.* 3D multifunctional integumentary membranes for spatiotemporal cardiac measurements and stimulation across the entire epicardium. *Nat. Commun.* **5**, 3329 (2014).
8. Chung, H. J. *et al.* Stretchable, multiplexed pH Sensors with demonstrations on rabbit and human hearts undergoing ischemia. *Adv. health. Mater.* **3**, 59-68 (2014).

9. Zhang, Z. *et al.* Near infrared laser-induced targeted cancer therapy using thermoresponsive polymer encapsulated gold nanorods. *J. Am. Chem. Soc.* **136**, 7317-7326 (2014).
10. Kim, J., Piao, Y. & Hyeon, T. Multifunctional nanostructured materials for multimodal imaging, and simultaneous imaging and therapy. *Chem. Soc. Rev.* **38**, 372-390 (2009).
11. Burns, A., Ow, H. & Wiesner, U. Fluorescent core-shell silica nanoparticles: towards “Lab on a Particle” architectures for nanobiotechnology. *Chem. Soc. Rev.* **35**, 1028-1042 (2006).
12. Phillips, E. *et al.* Clinical translation of an ultrasmall inorganic optical-PET imaging nanoparticle probe. *Sci. Transl. Med.* **6**, 260ra149 (2014).
13. Lee, J.-H. *et al.* Artificially engineered magnetic nanoparticles for ultra-sensitive molecular imaging. *Nat. Med.* **13**, 95-99 (2007).
14. Vivero-Escoto, J. L. *et al.* Silica-based nanoprobe for biomedical imaging and theranostic applications. *Chem. Soc. Rev.* **41**, 2673-2685 (2012).
15. Zhang, K., Hao, L., Hurst, S. J. & Mirkin, C. A. Antibody-linked spherical nucleic acids for cellular targeting. *J. Am. Chem. Soc.* **134**, 16488-16491 (2012).
16. Kuribara, K. *et al.* Organic transistors with high thermal stability for medical applications. *Nat. Commun.* **3**, 723 (2012).
17. Kim, D.-H. *et al.* Stretchable and foldable silicon integrated circuits. *Science* **320**, 507-511 (2008).

18. Kim, D.-H. *et al.* Epidermal electronics. *Science* **333**, 838-843 (2011).
19. Kaltenbrunner, M. *et al.* An ultra-lightweight design for imperceptible plastic electronics. *Nature* **499**, 458-463 (2013).
20. Sekitani, T., Zschieschang, U., Klauk, H. & Someya, T. Flexible organic transistors and circuits with extreme bending stability. *Nat. Mater.* **9**, 1015-2022 (2010).
21. Kim, K. S. *et al.* Large-scale pattern growth of graphene films for stretchable transparent electrodes. *Nature* **457**, 706-710 (2009).
22. Bae, S. *et al.* Roll-to-roll production of 30-inch graphene films for transparent electrodes. *Nat. Nanotech.* **5**, 574-578 (2010).
23. Lee, M.-S. *et al.* High-performance, transparent, and stretchable electrodes using graphene–metal nanowire hybrid structures. *Nano Lett.* **13**, 2814-2821 (2013).
24. Gallagher, F. A. *et al.* Magnetic resonance imaging of pH in vivo using hyperpolarized ¹³C-labelled bicarbonate. *Nature* **453**, 940-943 (2008).
25. Jana, N. R., Gearheart, L. & Murphy, C. J. Wet chemical synthesis of high aspect ratio cylindrical gold nanorods. *J. Phys. Chem. B.* **105**, 4065-4067 (2001).
26. Singh, N. *et al.* Bioresponsive mesoporous silica nanoparticles for triggered drug release. *J. Am. Chem. Soc.* **133**, 19582-19585 (2011).
27. Kim, S. *et al.* Bioresponsive mesoporous silica nanoparticles for triggered drug release. *Nat. Biotechnol.* **22**, 93-97 (2003).

28. Ling, D. *et al.* Multifunctional tumor pH-sensitive self-assembled nanoparticles for bimodal imaging and treatment of resistant heterogeneous tumors. *J. Am. Chem. Soc.* **136**, 5647-5655 (2014).
29. Yavuz, M. S. *et al.* Gold nanocages covered by smart polymers for controlled release with near-infrared light. *Nat. Mater.* **8**, 935-939 (2009).
30. Lee, H. *et al.* An endoscope with integrated transparent bioelectronics and theranostic nanoparticles for colon cancer treatment. *Nat. Commun.* **6**:10059 (2015).
31. Lee, H. Integrated electrochemical sensors and actuators for multifunctional surgical endoscope and glucose monitoring system. *Doctoral thesis in Graduate School of Seoul National University* (2016).

***Some contents of this chapter are published in *Nature Communications* (2015, 6:10059).**

Chapter 4. Localized delivery of theranostic nanoparticles and high-energy photons using microneedle-integrated bioelectronics for minimally-invasive cancer treatment

4.1 Introduction

Theranostic nanoparticles (NPs) which is activated by external stimuli have a huge potential for the cancer treatment, simultaneously minimizing critical side effects of the treatment on nearby normal tissues¹. The interaction between the theranostic NPs and stimuli actuates physicochemical changes of the theranostic NPs for the activation of theranostic agents. The theranostic NPs, especially for the light-responsive NPs, have been deeply studied. The easy control of the therapeutic agents enables localized treatment without serious side effects, for example thermal, chemical, or electrical damages on normal tissues²⁻⁴.

However, the theranostic NPs, especially for intravenously injected NPs, have the low efficiency of delivery to the tumors. It is a critical problem in case of brain tumors due to the blood-brain barrier (BBB)^{5,6}. BBB is a barrier to protect the central nervous system from harmful factors and it also hinders the theranostic NPs' delivery to the brain tissue. In spite of various advantages, the low efficiency of the NPs' delivery seriously restricts the efficacy of the

theranostic NPs. Therefore, a localized delivery method of the theranostic NPs avoiding BBB is required for the brain tumor treatment^{7,8}.

On the other hands, lights with long wavelength including red and/or near-infrared (NIR) light have been utilized for the activation of theranostic NPs using the lights due to the deep penetration depth to human tissues^{9,10}. However, they have low energy which is insufficient to completely activate theranostic functions. Although several approaches have been studied to solve the low energy problem including the upconversion method^{11,12}, their efficiency still requires further improvement. Therefore, this problem still remains as an important research field.

On behalf of the long-wavelength light, the lights with short wavelength including blue and ultraviolet (UV) light could have a high efficiency owing to the high energy¹³. Therefore, they could be a solution with high potent for the low energy issue of long-wavelength lights for the activation of theranostic NPs. For example, protoporphyrin and Ce6 which are representative photodynamic (PDT) dyes absorb the light still more effectively as activated by short-wavelength lights (~365 nm; 3.4 eV) than long-wavelength lights (~650 nm; 1.9 eV)^{14,15}. The delivery of high-energy photons into the deep tumor tissue, however, is challenging because of the scattering and absorption by biological tissues¹¹.

4.2 Experimental section

4.2.1 Fabrication of the microneedle mold

The microneedle mold is manufactured by using the commercial microneedle. The mixture of the prepolymer of polydimethylsiloxane (PDMS; SYLGARD™ 184, Dow Corning Corp., USA) and the curing agent (10:1 weight ratio for prepolymer:curing agent) is poured in a petri dish. The trapped air in the mixture is removed by vacuum. The commercial microneedle (PM001, Prestige Medicare, Republic of Korea) is put on the dish having the mixture, and it is cured on the hot plate with 100 °C. The commercial microneedle is pulled out, and the fabrication of PDMS mold is completed.

4.2.2 Preparing bioresorbable microneedles

The BMNs are fabricated by the molding process. 0.3 g of hyaluronic acid is mixed with the 4 mL of the 7.5 mM theranostic NPs for preparing the base solution. The base solution is completely mixed by a vortex mixer (Vortex-Genie 2, Scientific Industries, Inc., USA) and an ultrasound sonicator (JAC-2010P, Kodo Technical Research Co. Ltd, Republic of Korea). 1 mL of the base solution and 1 mL of deionized water (DW) are poured into the mold. The trapped air is eliminated by vacuum. 0.5 mL of DW is poured into the pre-mixed solution. Then, these procedure is repeated twice. Finally, water content in the solution is evaporated over 1 day.

4.2.3 Preparing light-guiding/-spreading microneedles

The LMNs are fabricated by the molding process similar to that of BMNs. 50 μL of acetone is mixed with 1 mL of the epoxy polymer solution (NOA63; Norland Optical Adhesive 63, Norland Products Inc., USA) to make the solution A. The alumina MPs which have a diameter of 1 μm and a concentration of $5 \times 10^8 \text{ cm}^{-3}$, are mixed to the solution A to prepare the solution B. These solutions are completely mixed by a vortex mixer and an ultrasound sonicator. The mold is filled with the solution B and the air inside the solution is removed by vacuum. The remained solution over the microneedle region in the mold is wiped out, and the solution in the microneedle region is cured by the UV light (Fusion Cure System, Minuta technology, Republic of Korea). The solution A is poured to the mold to prepare the substrate and the air inside is eliminated again. The solution A is cured by the same process for curing the solution B.

4.2.4 Animal experiment procedure by mouse tumor models

The mouse models for glioblastoma (GBM) and pituitary adenoma (PA) were prepared for demonstration of the proposed method. First, the mouse models were prepared 3 weeks after tumor implantation. The skin is incised to reveal tumor tissue and the BMNs were attached to the tumor. After 1 – 2 min, the BMNs were dissolved and the substrate of BMNs is removed. BMNs are attached 3 times to the different area of the tumors. The LMNs are attached to apply the UV photons to activate the theranostic NPs inside the tumor tissue. LMNs are attached 3 times to apply the light in the large area. Then, the BMNs'

substrate is applied to the previously treated area of the tumor, due to the insufficient amount of the NPs using only the BMNs during tumor treatment. After the BMNs' substrate is dissolved by using saline solution, UV light is irradiated by the bioelectronics for activation of the NPs delivered by the BMNs' substrate. The tumor tissue was fully covered by the bioglue (EVICEL, Ethicon, USA) to protect tumor and prevent the leakage of the chemo-drugs. As a final step, the skin was sutured and disinfected.

4.3 Results and discussion

4.3.1 Localized delivery of theranostic nanoparticles by microneedle-integrated bioelectronics

We present a localized delivery system of the theranostic NPs and high-energy photons to the tumor tissues (*e.g.*, GBM and PA) by microneedle-integrated bioelectronics. Bioresorbable and light-guiding/-spreading microneedles with the bioelectronics are integrated to the surgical forceps. Figure 4.1 shows an overall procedure of the localized delivery method.

First, bioresorbable microneedles (BMNs) which is made of hyaluronic acid and the theranostic NPs are applied to the target tumor (Fig. 4.1a). The BMNs are immediately dissolved by biofluids, and the theranostic NPs are delivered to the target region (Fig. 4.1b). Although the BBB inhibits the intravenous delivery to the brain tissue, the proposed method is not affected by the BBB and delivers the theranostic NPs to the tumor. Because of the thin thickness of forceps, this method minimizes the incision size, which reduces the consequent pain and recovery time.

Second, light-guiding/-spreading microneedles (LMNs) integrated with the bioelectronics are applied to the target tumor (Fig. 4.1c). The high-energy photons are irradiated from the UV light-emitting diode (LED) attached to the bioelectronics. LMNs deliver the generated photons to the pre-delivered NPs in the tumor tissue. The alumina microparticles (MPs) are contained in the LMNs, so the guided photons are delivered further to neighboring tumor tissues (Fig. 4.1d). Therefore, LMNs containing MPs not only guide but also diffuse

high-energy photons to the target tumor. These delivered photons induce activation of the theranostic NPs.

The theranostic NP is composed of an iron oxide core and a mesoporous silica shell. On the surface of the shell, PDT dyes are attached and photo-labile linkers are used to bond the chemo-therapy drugs (chemo-drugs). The iron oxide core can be used for the magnetic resonance (MR) imaging. As the high-energy photons are irradiated, the PDT dyes generate reactive oxygen species (ROS). And the photo-labile linkers are disconnected to release the chemo-drugs from the NP surface (Fig. 4.1e). The heat from the LED enhances the diffusion of therapeutic agents in the target tumor by enhancing the diffusivity as well as the permeability of the cell membrane^{16,17} (Fig. 4.1d).

Other than GBM, the localized delivery method can be used to another type of brain tumors including pituitary adenoma (PA; Fig. 4.1f). PA secretes an abnormal amount of hormones, which causes many complications^{18,19}. The minimally-invasive surgery is generally conducted to remove PA^{20,21}. In this procedure, a surgical endoscope with thin forceps is used for the monitor and removal of PA. However, the normal pituitary gland neighboring the PA can be damaged during the removal of PA due to the small size²⁰. The proposed method can avoid and minimize that a risk.

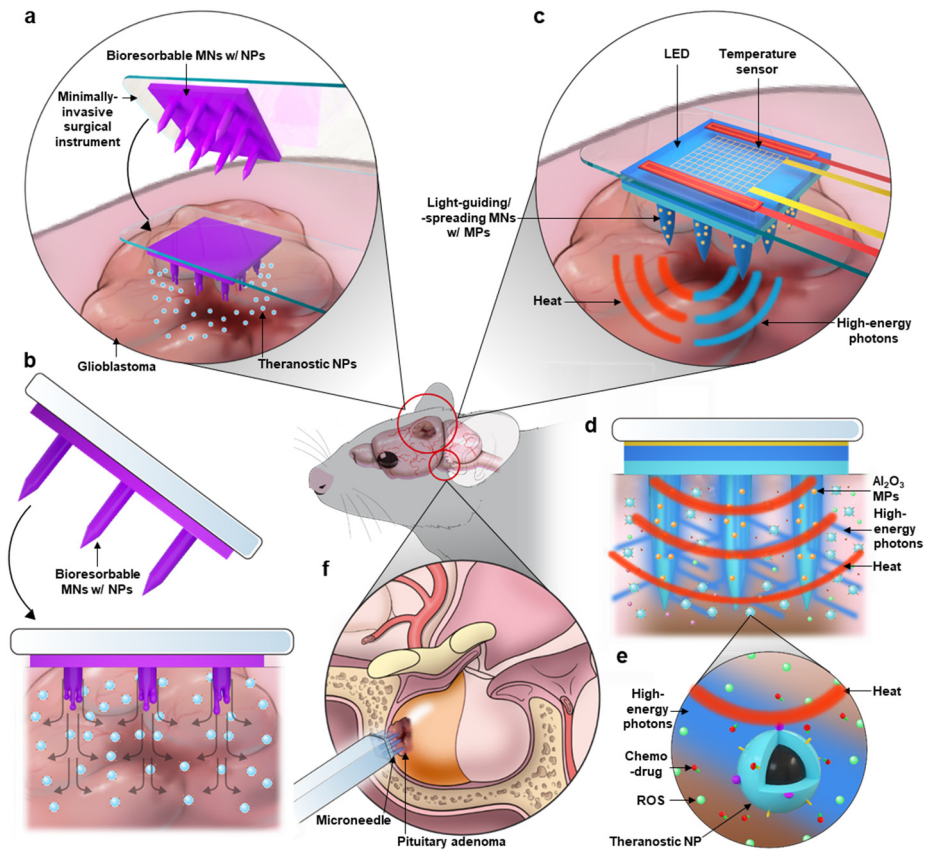


Figure 4.1. Localized delivery system of theranostic NPs and high-energy photons for brain tumor treatment. (a) Local delivery of the NPs to GBM using BMNs. **(b)** Biodegradation of the BMNs and release of the NPs into the target tumor. **(c)** Delivery of the high-energy photons using LMNs and the heat control by the bioelectronics. **(d)** The NPs activation by the high-energy photons and diffusion acceleration of the therapeutic agents by the thermal actuation. **(e)** Release of the ROS and chemo-drugs by the UV irradiation. **(f)** Application of the localized delivery method to the PA treatment.

4.3.2 Fabrication, design, and characterization of bioresorbable microneedles

The BMNs are prepared by the molding process (Fig. 4.2a). The base solution is composed of 0.3 g of hyaluronic acid and 4 mL of 2 mM theranostic NPs in DW. The base solution is filled in a needle mold and the air trapped in the mold is eliminated by vacuum. Then, the mold is completely filled with the solution. As water content in the solution is evaporated, BMNs are solidified. Finally, BMNs are pulled out from the mold. Details for preparing the BMNs and the mold are explained in Methods.

The BMN is have a dimension of 0.25×2 mm (diameter \times length; single microneedle) and an inter-needle space of 2 mm (Fig. 4.2b). The aspect ratio (length / diameter) of the BMN is 8. The fluorescence images of a BMN containing the PDT dyes (green) doped in the NPs and the chemo-drugs (*e.g.*, Doxorubicin (Dox); red) loaded on the NPs (Fig. 4.2c left and right, respectively) present the uniform distribution of the NPs in the needle. Also, the tip of the BMN has a sharp edge.

The BMNs are mechanically rigid enough to puncture the target tumor without damage on the BMNs during the penetration. The mechanical rigidity of the BMNs is evaluated by the compression test (Fig. 4.2d). Weights are put on the BMNs to apply the pressure along the vertical direction. The maximum pressures that the BMNs can endure is 13.8 MPa, which is high enough to be inserted to the tumor tissues (*e.g.*, brain tumor tissue whose Young's modulus is 11.4 kPa²²).

The BMNs are applied to the brain model that is made of 0.6% agar gel²³. The BMNs can penetrate the artificial tissue, which demonstrates the mechanical strength of BMNs (Fig. 4.2e). After the BMNs penetrate the artificial tissue, the tip of BMN is dissolved in 1 – 2 min (Fig. 4.2f). As applying high-energy photons (3.4 eV) to the released NPs after the BMN is dissolved, the chemo-drugs (*e.g.*, Dox) are released from the NPs. Figure 3.2g shows the diffusion of the chemo-drugs to the artificial brain tissue using the UV light irradiation for 20 min at 37 °C. Chemo-drugs (red fluorescence) are shown in the NPs without the UV light irradiation (Fig. 4.2g left), whereas they are released to the neighboring artificial tissue by the UV light irradiation (Fig. 4.2g right).

The chemo-drugs released from the NPs can be naturally diffused owing to the concentration gradient. Still, that mass transfer based the diffusion is too slow. The mass transfer can be enhanced dramatically by the thermal actuation. The measurement setup and the focusing position for the observation of the chemo-drug diffusion are presented in Figs. 4.2h and 4.3. Figure 4.2i,j show the diffused chemo-drugs (red fluorescence) under 37 °C and 47 °C after 20 min (Fig. 4.2i and Fig. 4.2j, respectively). The chemo-drugs diffusion is quite slow at 37 °C, so the inter-needle space is partially filled by the chemo-drugs (Fig. 4.2i). However, the thermal actuation ($\Delta T = 10$ °C) can enhance the drug diffusion so that the chemo-drugs can be more diffused and rapidly fill the inter-needle space (Fig. 4.2j).

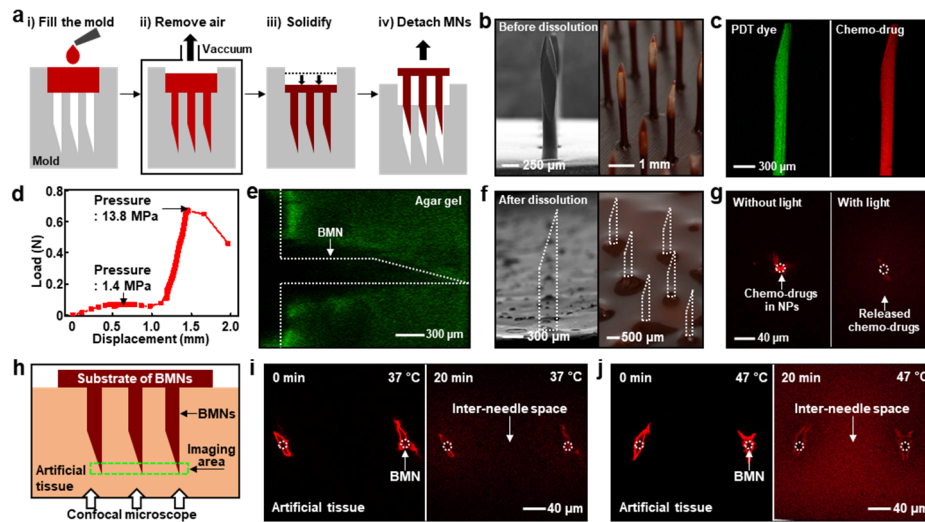


Figure 4.2. Fabrication, design, and characterization of BMNs. (a) Schematic illustrations for the fabrication of BMNs. (b) Scanning electron microscope (SEM; left) and camera (right) image of BMNs. (c) Fluorescence microscope image of PDT dyes (left) and that of chemo-drugs (right) in the theranostic NPs which is contained in the BMNs. (d) Mechanical strength test (load-displacement curve) of the BMNs by using the weights on the BMNs. (e) Fluorescence microscope image of a BMN that is applied to the artificial brain. (f) SEM (left) and camera (right) image of the BMN after dissolution. (g) Release and diffusion of chemo-drugs (*e.g.*, Dox) from the NPs without (left) and with (right) the UV light irradiation using the bioelectronics. (h) Measurement area of the fluorescence image to evaluate the chemo-drug diffusion. (i,j) Fluorescence microscope images for the evaluation of the drug diffusion in the artificial tissue using the UV light irradiation for 20 min at 37 °C i and 47 °C j. The inter-needle space of the BMNs are partially (37 °C) and completely (47 °C) filled by the chemo-drugs.

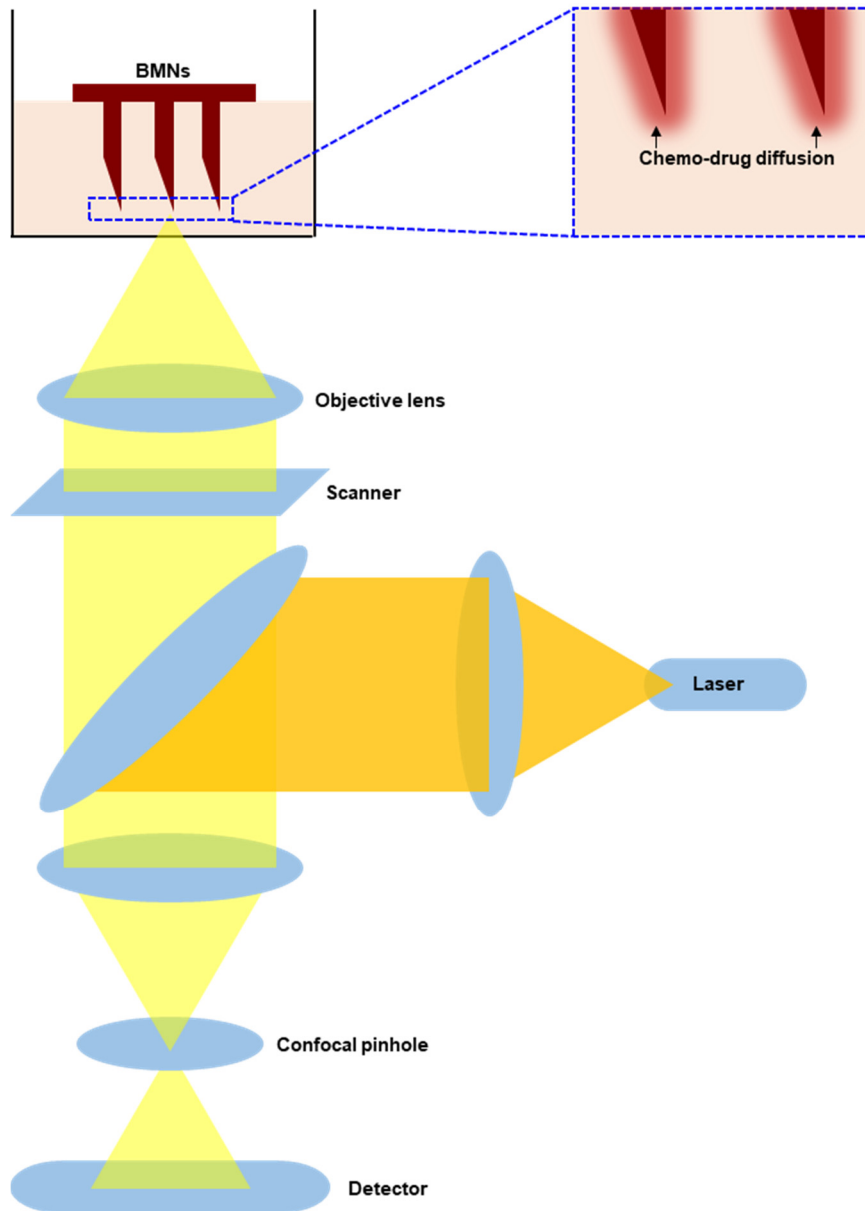


Figure 4.3. Fluorescence measurement setup and focusing position. Fluorescence measurement setup for the confocal microscope imaging for the evaluation of the drug diffusion in the artificial brain. The magnified cartoon presents the focusing position for the evaluation of the chemo-drug diffusion.

4.3.3 Characterization of light-guiding/-spreading microneedles

The LMNs consist of a transparent polymer (epoxy; NOA63, Norland Products Inc., USA), and alumina MPs are contained in the LMNs (Fig. 4.4a,b). The preparing LMNs is similar to that of BMNs. Detailed fabrication process is described in Methods. The LMNs have a dimension of 0.3×3 mm (diameter \times length) and an inter-needle space of 2 mm. The alumina MPs have a diameter of 1 μm and a refractive index of 1.8. The LMNs deliver and diffuse UV photons into the tumor tissue. The UV photons can be delivered to the theranostic NPs inside the target tumor tissue.

The alumina MPs contained inside the LMNs enhance the scattering of the UV photons. As reported by the optical simulation, the alumina MPs make strong scattering (*i.e.*, Mie scattering) of the UV light (wavelength: 365 nm; Fig. 4.4c)²⁴. More detailed methods about the optical simulations including the development of the model are explained in Methods and Fig. 4.5. Owing to the scattering of the UV photons, the irradiated photons can be spread more to neighboring theranostic NPs.

Providing the design of MPs and LMNs, the delivered light flux can be varied. For instance, the delivered light power varies by the refractive index, size, and concentration of the MPs (Fig. 4.4d,e). The optimized parameters of the MP are calculated for the maximum light energy, *i.e.*, a refractive index of 1.8, a diameter of 1 μm , and a concentration of $5 \times 10^8 \text{ cm}^{-3}$. Figure 4.4f and Fig. 4.6 exhibit the simulated light flux delivered to the tissue using LMNs depending on the length of LMNs (with 365 nm UV light). Because the total

light energy and the penetration depth are enhanced with the longer length of the LMN, the longest LMN (3 mm-long) is chosen.

The LMNs containing MPs with the optimum design extremely enhance the light flux delivered into the tissue. The simulated flux of the light through the LMN is higher than the control groups (*i.e.*, UV or NIR delivery without LMNs), especially at the deep tissue (Fig. 4.4g). For instance, Fig. 4.4h shows the 3D light distributions: 1) UV delivery without the LMNs (control), 2) NIR delivery without the LMNs (control), and 3) UV delivery via the LMNs with the MPs. The high-energy photons cannot reach to ~1 mm without LMNs owing to the high scattering and absorption by the brain tissue. The NIR photons penetrate ~2 mm, because the low scattering and absorption of the NIR light compared to the UV light. In spite of the deeper penetration, the energy of NIR light is still lower than that of UV, so the energy for the activating NPs is insufficient^{25,26}. Besides, the LMN containing the MPs guides the high-energy photons to much deeper area (~3 mm), even more than the NIR case. Moreover, the energy of the high-energy photons is higher than that of the NIR photons. Figure 4.4i presents the experimental results of the cases. Optical phantoms are applied for the experiment. Corresponding to simulation results, the LMN containing MPs presents the deepest delivery of the light. Therefore, the activation of the theranostic NPs at the deep tissue can be made by the UV photons guided by the LMNs containing alumina MPs. See Methods for details about the optical measurement and the fabrication of the optical phantoms.

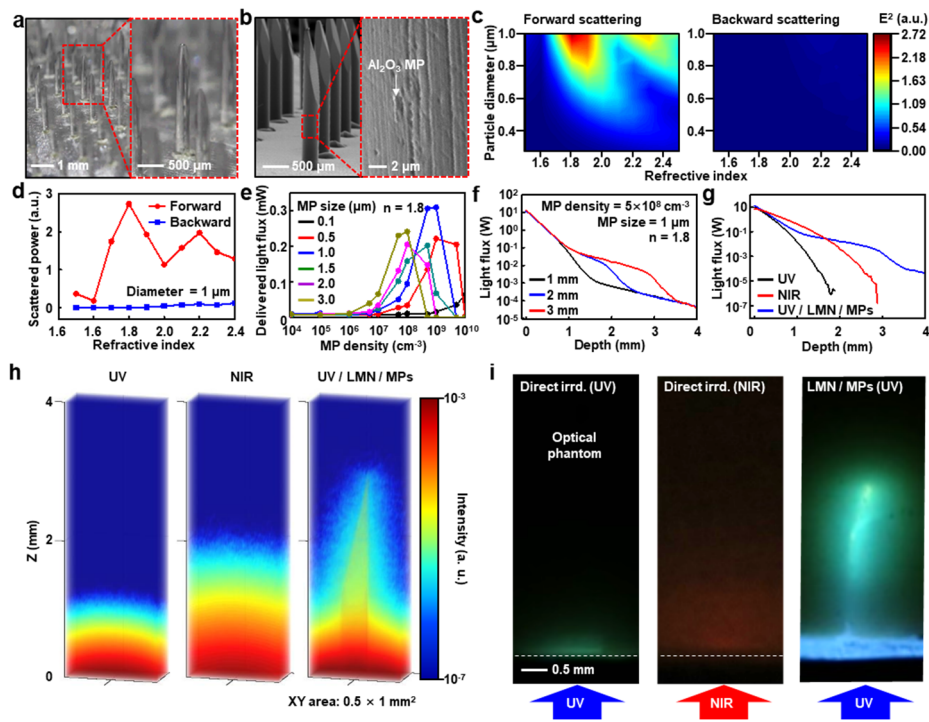


Figure 4.4. Characterization of LMNs. (a) Optical images of LMNs. (b) SEM images of LMNs. (c) Calculated forward and backward scattering using the alumina MPs depending on various refractive indices and diameters. (d) Calculated light flux depending on the refractive index of the alumina MP. (e) Calculated light flux depending on the density and size of the alumina MPs. (f,g) Calculated depth profile of the delivered light energy in the brain depending on the length of the LMN f and the type and method of the light g. (h) Calculated 3D visualization of the light delivery to the brain depending on the type and method of the light delivery. (i) Optical images of the artificial phantom with the direct UV irradiation without LMNs (left), the direct NIR irradiation without LMNs (middle), and the UV delivery through LMNs with alumina MPs (right).

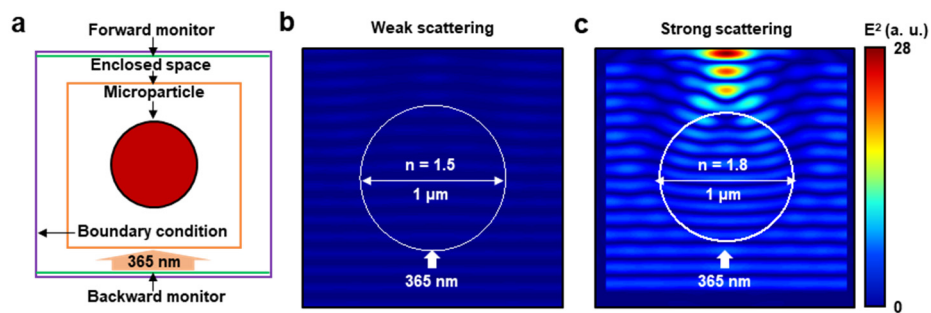


Figure 4.5. Simulation model and results for the light scattering by the alumina MP contained in the LMNs. (a) Simulation model for the light scattering by the alumina MP. **(b,c)** Scattering of the UV photons (365 nm wavelength) by the alumina MP having a refractive index of 1.5 **(b; weak scattering)** and 1.8 **(c; strong scattering)**.

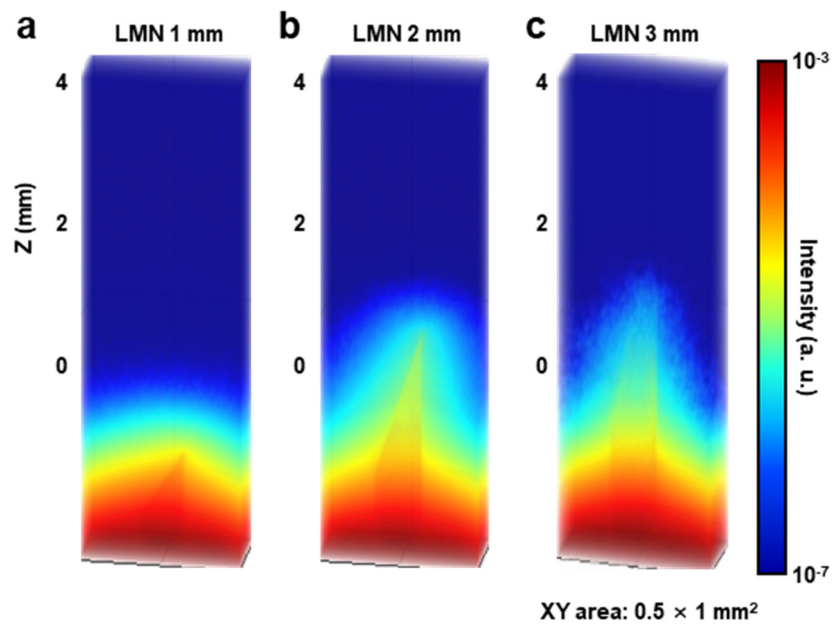


Figure 4.6. Calculated 3D visualization of the light distribution depending on the LMN length. (a-c) 3D light distribution in the brain tissue guided by the LMNs, whose length is 1 mm (a), 2 mm (b), and 3 mm (c).

4.3.4 LMNs and bioelectronics integrated with microneedles

The LMNs and flexible bioelectronics are integrated on the surgical forceps for the minimally-invasive treatment of cancer. The LMNs and the device can be integrated on the different position such as the tip and/or the side of the surgical forceps depending on their applications (Figs. 4.7a and 4.8, respectively). The bioelectronics are composed of LMNs, an LED, a temperature sensor, electrical interconnects, and wiring pads. The LMNs are attached on the LED of the bioelectronics for the deep penetration depth of generated photons to the target tumor (Fig. 4.7a inset). The temperature sensor in the bioelectronics is integrated directly under the LED to precisely monitor the heat generated by the LED.

The device is prepared by microfabrication processes. In brief, Au is deposited and patterned on a bottom encapsulation layer (polyimide) for the temperature sensor. Cu is deposited and patterned to build the LED interconnection. Top encapsulation layer is coated and entire layers are etched. Then, the LMNs are applied to the LED and the device is transfer to the surgical forceps. The heat from the LED is utilized to enhance the diffusion of the theranostic agents, which can be precisely controlled by the temperature sensor. See Fig. 4.8b,c for detailed designs of the bioelectronics. Also, more details about the fabrication is shown in Fig. 4.9.

Figure 4.7b presents the light intensity depending on the wavelength of the light emission from the LMNs on the LED (blue curve) and the light absorbance from the theranostic NPs (red curve). The peak wavelengths for the

light emission and absorption well overlap each other. Therefore, the UV photons delivered by LMNs sufficiently activate the theranostic NPs for cancer treatment (Fig. 4.7b). The current applied to the LED and the light intensity from the LED is linearly correlated (Fig. 4.7c), so the light intensity can be easily controlled.

The electrical energy applied to LED is converted to the light and heat simultaneously. The heat from LED can be used to raise the temperature of the target tissue by controlling the current for the LED (Fig. 4.7d). The target temperature (~ 47 °C) can be achieved by applying the current of 200 – 240 mA (Fig. 4.10a). The temperature sensor is calibrated (Fig. 4.10b) and monitors the temperature of the target tissue during the light irradiation (Fig. 4.10c). The time to achieve the steady state of thermal balance was less than 1 min (Fig. 4.10d). The temperature control using the temperature sensor facilitate the repetitive turn-on/-off of the thermal actuation (Fig. 4.7e).

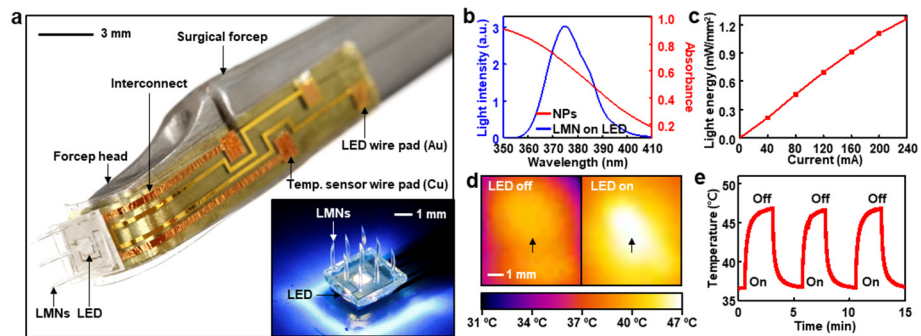


Figure 4.7. Characterization of LMN-integrated bioelectronics. (a) LMN-integrated bioelectronics on the tip of surgical forcep. The inset image shows the light irradiation through LMNs attached on the UV LED. **(b)** Light intensity measurement depending on the wavelength of generated light from the LED and the light absorption by the theranostic NPs. **(c)** Control of light energy depending on the current applied to the LED. **(d)** Infrared images of the artificial brain tissue as the LED is turned on (right) and off (left). **(j)** Measurement of cyclic temperature change.

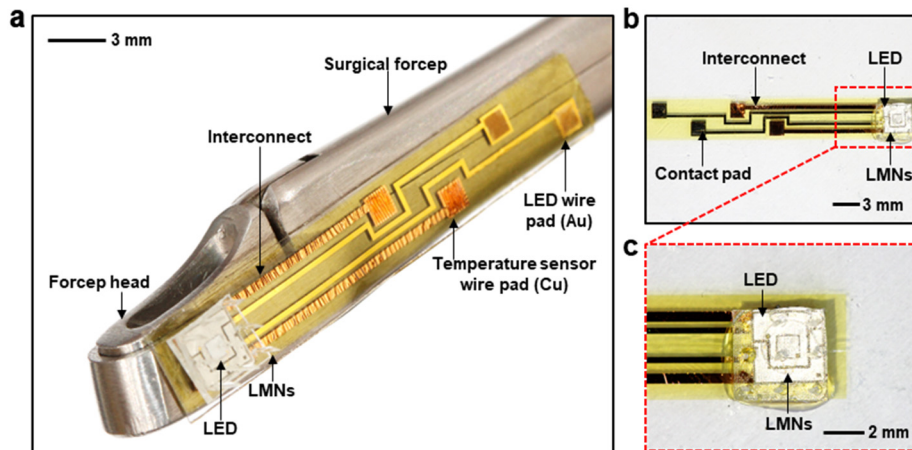


Figure 4.8. Optical camera images of the bioelectronics. (a) The microneedle-integrated bioelectronics on the side of the surgical forcep. **(b)** Detailed design image (top view) of the bioelectronics. **(c)** Magnified image of the LED and LMNs.

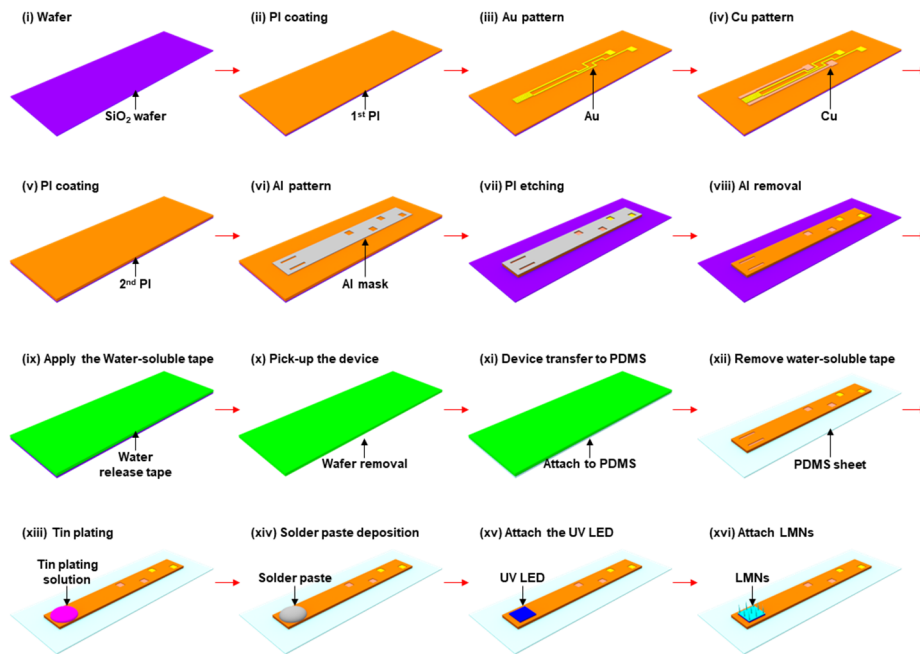


Figure 4.9. Step-by-step fabrication and integration process of the bioelectronics. Schematic illustrations for the fabrication procedures including the microfabrication, integration, wiring pad fabrication, and integration of the bioelectronics with the LMNs.

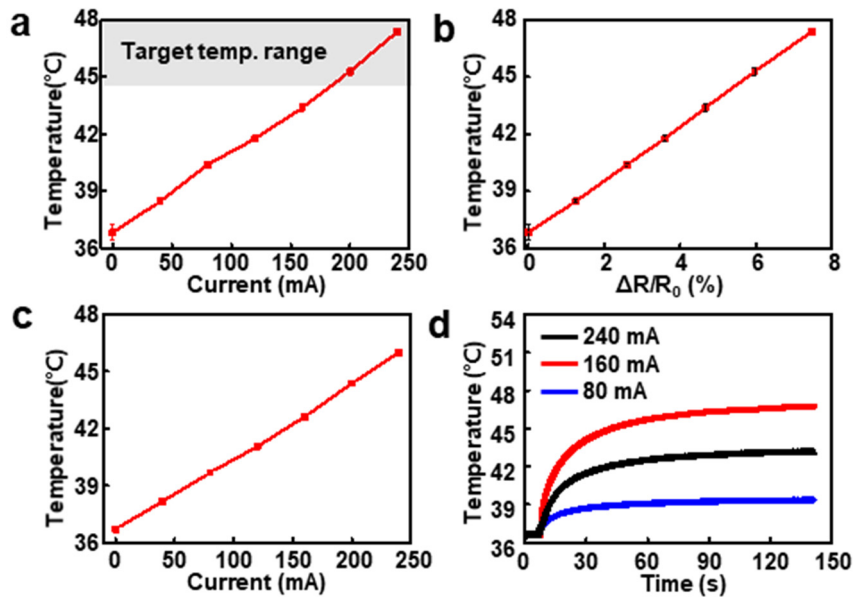


Figure 4.10. Characterizations of the temperature monitoring by the bioelectronics. (a) Temperature change of the artificial brain tissue with various applied current for the thermal actuation. (b) Calibration graph of the temperature sensor. (c) Temperature variation of the artificial tissue detected by the temperature sensor in the bioelectronics for the thermal actuation. (d) Temperature variation of the artificial brain tissue for the thermal actuation monitored by the temperature sensor in the bioelectronics for different applied currents to the LED.

4.4 Conclusion

We have developed a localized delivery method of theranostic NPs and high-energy photons using the microneedle-integrated bioelectronics for minimally-invasive cancer treatment. Using the proposed system, we evaluated the delivery of the therapeutic NPs for the brain cancer treatment. The NPs were locally diffused from BMNs to the cancer region and activated with the UV photons delivered by LMNs integrated on the bioelectronics. After activation, the theranostic NPs release the ROS and chemo-drugs for localized cancer treatment. The thermal actuation by using the bioelectronics enhanced the diffusion of the therapeutic agents. This novel delivery method of the theranostic NPs and high-energy photons has a huge potential for the next-generation bioelectronics²⁹⁻³² for minimally-invasive cancer treatment. Further studies for the the microneedle designs and the application experiments with larger animals are needed in the future.

References

1. Merino, S., Martín, C., Kostarelos, K., Prato, M. & Vázquez, E. Nanocomposite Hydrogels: 3D Polymer–Nanoparticle Synergies for On-Demand Drug Delivery. *ACS Nano* **9**, 4686–4697 (2015).
2. Lee, H. *et al.* An endoscope with integrated transparent bioelectronics and theranostic nanoparticles for colon cancer treatment. *Nat. Commun.* **6**, 10059 (2015).
3. Yoo, S. W. *et al.* Endoscopic non-ablative fractional laser therapy in an orthotopic colon tumor model. *Sci. Rep.* **8**, 1673 (2018).
4. Bansal, A., Yang, F., Xi, T., Zhang, Y. & Ho, J. S. In vivo wireless photonic photodynamic therapy. *Proc. Natl. Acad. Sci.* **115**, 1469–1474 (2018).
5. Banks, W. A. From blood–brain barrier to blood–brain interface: new opportunities for CNS drug delivery. *Nat. Rev. Drug Discov.* **15**, 275–292 (2016).
6. Arvanitis, C. D., Ferraro, G. B. & Jain, R. K. The blood–brain barrier and blood–tumor barrier in brain tumors and metastases. *Nat. Rev. Cancer* **20**, 26–41 (2020).
7. Nam, L. *et al.* Drug Delivery Nanosystems for the Localized Treatment of Glioblastoma Multiforme. *Materials (Basel)*. **11**, 779 (2018).
8. Stephen, Z. R. *et al.* Redox-Responsive Magnetic Nanoparticle for Targeted Convection-Enhanced Delivery of O⁶-Benzylguanine to Brain Tumors. *ACS Nano* **8**, 10383–10395 (2014).

9. Wang, H. *et al.* Targeted production of reactive oxygen species in mitochondria to overcome cancer drug resistance. *Nat. Commun.* **9**, 562 (2018).
10. Li, L. *et al.* A Rationally Designed Semiconducting Polymer Brush for NIR-II Imaging-Guided Light-Triggered Remote Control of CRISPR/Cas9 Genome Editing. *Adv. Mater.* **31**, 1–9 (2019).
11. Chu, H., Zhao, J., Mi, Y., Di, Z. & Li, L. NIR-light-mediated spatially selective triggering of anti-tumor immunity via upconversion nanoparticle-based immunodevices. *Nat. Commun.* **10**, 2839 (2019).
12. Liu, J., Bu, W., Pan, L. & Shi, J. NIR-Triggered Anticancer Drug Delivery by Upconverting Nanoparticles with Integrated Azobenzene-Modified Mesoporous Silica. *Angew. Chemie Int. Ed.* **52**, 4375–4379 (2013).
13. Kim, M. *et al.* Optical lens-microneedle array for percutaneous light delivery. *Biomed. Opt. Express* **7**, 4220 (2016).
14. HATAKEYAMA, T. *et al.* Efficacy of 5-aminolevulinic acid-mediated photodynamic therapy using light-emitting diodes in human colon cancer cells. *Oncol. Rep.* **29**, 911–916 (2013).
15. Martynenko, I. V. *et al.* Energy transfer in complexes of water-soluble quantum dots and chlorin e6 molecules in different environments. *Beilstein J. Nanotechnol.* **4**, 895–902 (2013).
16. Lee, J. *et al.* Flexible, sticky, and biodegradable wireless device for drug delivery to brain tumors. *Nat. Commun.* **10**, 5205 (2019).

17. Bischof, J. C. *et al.* Dynamics of cell membrane permeability changes at suprphysiological temperatures. *Biophys. J.* **68**, 2608–2614 (1995).
18. Asa, S. L. & Ezzat, S. The pathogenesis of pituitary tumors. *Nat. Rev. Cancer* **2**, 836–849 (2002).
19. Beckers, A., Petrossians, P., Hanson, J. & Daly, A. F. The causes and consequences of pituitary gigantism. *Nat. Rev. Endocrinol.* **14**, 705–720 (2018).
20. Gondim, J. A. *et al.* Endoscopic endonasal approach for pituitary adenoma: surgical complications in 301 patients. *Pituitary* **14**, 174–183 (2011).
21. Di Ieva, A., Rotondo, F., Syro, L. V., Cusimano, M. D. & Kovacs, K. Aggressive pituitary adenomas—diagnosis and emerging treatments. *Nat. Rev. Endocrinol.* **10**, 423–435 (2014).
22. Chauvet, D. *et al.* In Vivo Measurement of Brain Tumor Elasticity Using Intraoperative Shear Wave Elastography. *Ultraschall der Medizin - Eur. J. Ultrasound* **37**, 584–590 (2015).
23. Chen, Z.-J. *et al.* A realistic brain tissue phantom for intraparenchymal infusion studies. *J. Neurosurg.* **101**, 314–322 (2004).
24. Wriedt, W. H. T. *The Mie Theory-Basics and Applications.* Springer (2012). doi:10.1007/978-0-387-34755-4{ }5.
25. Sun, L., Ma, X., Dong, C.-M., Zhu, B. & Zhu, X. NIR-Responsive and Lectin-Binding Doxorubicin-Loaded Nanomedicine from Janus-Type Dendritic PAMAM Amphiphiles. *Biomacromolecules* **13**, 3581–3591

- (2012).
26. de Gracia Lux, C. *et al.* Single UV or Near IR Triggering Event Leads to Polymer Degradation into Small Molecules. *ACS Macro Lett.* **1**, 922–926 (2012).
 27. Fukuoka, H. *et al.* EGFR as a therapeutic target for human, canine, and mouse ACTH-secreting pituitary adenomas. *J. Clin. Invest.* **121**, 4712–4721 (2011).
 28. Murasawa, S. *et al.* Inhibitory effects of SOM230 on adrenocorticotrophic hormone production and corticotroph tumor cell proliferation in vitro and in vivo. *Mol. Cell. Endocrinol.* **394**, 37–46 (2014).
 29. Park, S. *et al.* One-step optogenetics with multifunctional flexible polymer fibers. *Nat. Neurosci.* **20**, 612–619 (2017).
 30. Zhang, Y. *et al.* Battery-free, lightweight, injectable microsystem for in vivo wireless pharmacology and optogenetics. *Proc. Natl. Acad. Sci.* **116**, 21427–21437 (2019).
 31. Acarón Ledesma, H. *et al.* An atlas of nano-enabled neural interfaces. *Nat. Nanotechnol.* **14**, 645–657 (2019).
 32. Gong, S. *et al.* A wearable and highly sensitive pressure sensor with ultrathin gold nanowires. *Nat. Commun.* **5**, 3132 (2014).

***Some contents of this chapter will be published in a scientific journal**

요약 (국문초록)

진단 및 치료를 위한 부드러운
바이오소자를 기반으로 한 생체
삽입가능하고 최소 침습적인
약물전달 시스템

이영식

화학생물공학부

에너지환경화학융합전공

대학원

서울대학교

바이오메디컬소자, 특히 특정 인체 부위에 적용되는 약물 전달 시스템은 다양한 임상 문제를 해결할 수 있는 돌파구를 제시하기 때문에 과학자들과 임상의학자들에게 상당한 관심을 끌었다. 기존의 재료 및 소자들은 단단하고 부피가 큰 특징 때문에 소자와 인체 사이의 기계적 불일치가 해당 조직에 심각한 손상을 일으킨다. 이와 관련하여, 부드러운 기능성 재료와 새로운 소자 디자인 전략,

그리고 임상적으로 관련된 시스템 수준의 적용은 이 분야의 빠른 성장을 가속화시켰다. 우리는 질병 진단 및 치료를 위해 부드러운 바이오전자소자를 사용해 세 가지 다른 유형의 생체 삽입형 및 최소 침습적인 약물전달 시스템을 소개한다.

먼저, 웨어러블 기기와 무선으로 연결된 부드러운 소형화된 약물 전달 삽입소자를 개발했다. 약물 전달 삽입소자는 전기 생리학적 신호를 지속적으로 모니터링하고 웨어러블 기기로부터 무선 전력 전송을 통해 전원이 공급된다. 피부에서의 전기 생리학적 신호 모니터링에 기반한 약물의 피하 방출은 간질 중첩증과 같은 긴급한 의료 상황에 대처할 수 있다.

둘째, 투명한 그래핀 바이오전자소자와 치료용 나노입자를 통한 다기능성 내시경 기반 수술 시스템이 개발되었다. 이러한 진보된 바이오전자소자 및 나노입자는 대장암 치료를 위한 폐쇄 루프 솔루션의 기초 기술로써, 형광 기반 암 조직 매핑, 임피던스 및 pH 측정, 접촉 및 온도 모니터링, 그리고 고주파 전기소작 및 국소적인 광역동 치료와 항암요법을 종합적으로 가능하게 한다.

셋째, 최소 침습적인 암 치료를 위해 마이크로니들이 통합된 바이오전자소자를 사용하여 암을 목표로 하는 치료용 나노입자와 고에너지 광자의 국소적인 전달 방법이 개발되었다. 치료용 나노입자는 생흡수성 마이크로니들에 의해 국소적으로 암조직을 목표로 전달된다. 그 후, 빛을 전달하는 마이크로니들은

바이오전자소자로부터 나오는 고에너지 광자를 전달한다. 이 고에너지 광자는 목표 암조직에서 광역동 치료 및 항암치료를 실행하기 위해 나노입자를 국소적으로 활성화시킨다.

주요어: 바이오전자소자, 생체삽입, 최소침습, 웨어러블, 약물전달, 진단, 치료

학번: 2013-22532